Two-dimensional Sisyphus cooling

Yvan Castin,[1] Kirstine Berg-Sørensen,[2] Jean Dalibard,[1] and Klaus Mølmer[2]
[1]*Laboratoire Kastler Brossel, Ecole Normale Supérieure, 24 rue Lhomond, F-75231 Paris Cedex 05, France*
[2]*Institute of Physics and Astronomy, Århus University, 8000 Århus C, Denmark*
(Received 15 March 1994)

We present theoretical descriptions of Sisyphus cooling in a two-dimensional laser configuration, based on semiclassical as well as quantum approaches. A detailed comparison of these various approaches and a discussion of their range of validity are given. Features of the cooled atomic distribution such as channeling of the atoms along specific lines in momentum space and the observability of tunneling induced resonances in the population of the ground state of the atomic motion in the optical potential wells are discussed.

PACS number(s): 32.80.Pj, 42.50.Vk

I. INTRODUCTION

In the last decade, a large amount of both experimental and theoretical work has been performed in order to study the processes involved in laser cooling of atoms [1,2]. In "optical molasses," the minimum temperatures that have been obtained experimentally are in the range 1–10 μK and they correspond to rms atomic momenta of the order of only a few photon momenta $\hbar k$ [3,4]. Theoretically it has been possible to give an account for such low temperatures in one-dimensional (1D) configurations, for which cooling mechanisms can be clearly identified and analyzed [5,6]. In 2D and 3D, extensive numerical calculations have been performed only in a regime where the internal atomic variables can be adiabatically eliminated leading to a Fokker-Planck-type equation for the classical atomic center-of-mass motion [7,8]. However, this approximation is not necessarily justified, as observed from a comparison between the Fokker-Planck approach and a full quantum treatment in 1D [6].

In the present paper, we present a theoretical analysis of a 2D molasses configuration, for which cooling occurs because of the Sisyphus effect [5]. This analysis involves a semiclassical treatment, without elimination of the atomic internal state, and different quantum treatments. We consider an atom for which the cooling transition involves the ground state, with angular momentum $J_g = 1/2$ and an excited level with angular momentum $J_e = 3/2$. The two ground sublevels g_+ and g_- have periodic potential energies $U_\pm(x,y)$ induced by the coupling between the atom and the laser field. The atom-laser coupling also gives rise to optical pumping processes, transferring the atom back and forth between the sublevels g_+ and g_-. Sisyphus cooling originates from the difference between U_+ and U_- and from the correlation between the spatial modulation of $U_\pm$ and optical pumping processes. For example, an atom in state g_+ is preferentially transferred to g_- by optical pumping processes in a place where U_+ is larger than U_-. Therefore an atom initially in state g_+ has to climb a potential hill for U_+ and it then jumps to g_- around the top of this U_+-potential hill. It is then put in a valley for U_- and it has to climb again a U_--potential hill before having an appreciable probability of being transferred back to g_+. These changes of Zeeman sublevels lead to a transfer of atomic potential energy into fluorescence field energy and they are the key dissipative element of the Sisyphus mechanism.

The laser-field configuration we consider consists of two standing waves along the x and y axes, linearly polarized in the y and x directions, and with a phase difference α:

$$\vec{E}(x,y,t) = 2E_0\vec{e}_y \cos kx \cos(\omega_L t) + 2E_0\vec{e}_x \cos ky \cos(\omega_L t + \alpha) \; . \qquad (1)$$

This configuration has been studied experimentally by Hemmerich and Hänsch [9]. Also one of us [7] and Finkelstein, Guo, and Berman [10] have calculated, after elimination of the internal state, the semiclassical force acting on a slowly moving atom in this configuration. The same analytical dependence on the atom-laser parameters were recovered for the friction and diffusion coefficients as in the 1D case. Such an approach, however, relies on an adiabatic elimination of the internal state, which is not generally valid. This becomes particularly obvious in the present laser configuration because of a divergence of the friction coefficient [7,10] in the vicinity of the nodes of the electric field (1). A derivation of the steady-state atomic distribution using a semiclassical force would then be technically difficult. The various treatments of the present paper do not rely on the elimination of the internal atomic state. They are therefore free of any singularity around the field nodes. In fact we find that the cooling process is dominated by the dynamics around the antinodes where the atomic density is maximal.

First quantum results for this 2D configuration have already been published in [11]. They have been obtained in the limit of large detunings between the laser and the atomic frequencies by the secular method. This method consists in calculating the steady-state populations of the various eigenstates of the Hamiltonian describing the atomic motion in $U_\pm(x,y)$. A remarkable feature of these

results was the existence of resonances in these populations as a function of the amplitude of $U_{\pm}$. They are due to the resonant tunneling between adjacent potential wells of $U_{\pm}$. These resonances were not present in the 1D configurations studied before and their observation would constitute a novel demonstration of the quantum nature of atomic motion in optical molasses.

In the large detuning limit, the theoretical treatment of laser cooling is simplified because optical pumping processes can be treated perturbatively, but this limit is hard to reach in practice. The observability of the resonances could not be easily deduced from the perturbative treatment of [11]. The purpose of this paper is to give a more complete study of the proposed 2D cooling configuration and to investigate in particular the sensitivity of the tunnel-induced resonances to laser detuning.

The paper is organized as follows. In the next section we derive the master equation describing the 2D atomic motion in the light field. We also introduce a modification of spontaneous emission which simplifies the calculations. In Sec. III the quantum equations are approximated by a classical stochastic process. Section IV presents our method of numerical integration of the full quantum equations of motion. Section V is devoted to a detailed presentation of the secular method. Finally, Sec. VI summarizes and compares the results obtained with these various methods.

II. MASTER EQUATION

A. The light-shift potential and the relaxation

In this paper, we restrict ourselves to laser fields with a saturation parameter $s_0 \ll 1$, which is known to lead to the lowest temperatures. The parameter

$$s_0 = \frac{2\Omega^2}{\Gamma^2 + 4\delta^2} \tag{2}$$

involves the Rabi frequency $\Omega = dE_0/\hbar$ characterizing the coupling between the atomic dipole d and the field amplitude E_0 of each traveling wave, the natural width Γ of the atomic excited state, and the detuning $\delta = \omega_L - \omega_A$ between the laser (ω_L) and atomic (ω_A) frequencies.

It is then possible to eliminate adiabatically the atomic excited state and to write down an equation of evolution for the restriction of the density operator to the atomic ground state [12,13]. The general form for this master equation is

$$\frac{d\rho}{dt} \equiv \mathcal{L}[\rho] = \frac{i}{\hbar}[\rho, H] + (\dot{\rho})_{\text{relax}}. \tag{3}$$

In (3), the Hamiltonian H describes the motion of the atom in the potential associated with the light shifts of the various ground-state sublevels. The light-shift amplitude scales as $\hbar\delta s_0$ and the spatial periodicity of the potential is related to the laser wavelength $\lambda = 2\pi/k$, so that H can be written

$$H = \frac{p^2}{2M} + 4\hbar\delta s_0 V(k\vec{r}) \ , \tag{4}$$

where $\vec{r}$ and $\vec{p}$ are the position and momentum operators for the atomic center of mass. For a fixed value of $\vec{r}$, V is an operator acting in the Hilbert space of the internal atomic ground level.

For the particular laser configuration studied here (1), the electric field lies in the x-y plane and it has only σ_+ and σ_- components when expanded in the standard basis associated with the z axis. Consequently V is diagonal in the basis $|g_{\pm}\rangle = |g, m_z = \pm 1/2\rangle$:

$$V(k\vec{r}) = \begin{pmatrix} V_+(k\vec{r}) & 0 \\ 0 & V_-(k\vec{r}) \end{pmatrix} . \tag{5}$$

Using the Clebsch-Gordan coefficients for a $J_g = 1/2 \leftrightarrow J_e = 3/2$ transition, we find that the elements $V_{\pm}$ are proportional to $I_{\pm} + (1/3)I_{\mp}$, where $I_{\pm} = |\mathcal{E}_{\pm}|^2$ are the intensities of the reduced $\sigma_{\pm}$ components $\mathcal{E}_{\pm}$ of the field:

$$\mathcal{E}_{\pm}(kx, ky) = \sqrt{2}(ie^{i\alpha}\cos kx \mp \cos ky) \ . \tag{6}$$

We then get

$$V_{\pm}(kx, ky) = \frac{1}{3}(\cos^2 kx + \cos^2 ky \pm \cos kx \cos ky \sin\alpha) \ . \tag{7}$$

As we have mentioned in the Introduction, Sisyphus cooling occurs if the two potentials $V_{\pm}$ have different spatial variations. This requires that $\sin\alpha \neq 0$. In the following we will give numerical results only in the case $\alpha = \pi/2$.

The relaxation part in (3) corresponds to transitions between atomic ground-state sublevels due to absorption–spontaneous-emission cycles. The rate of these optical pumping transitions scales as Γs_0 and we therefore write

$$(\dot{\rho})_{\text{relax}} = \Gamma s_0 \mathcal{L}_{\text{relax}}(\rho, k\vec{r}). \tag{8}$$

For the particular geometry studied here, the relaxation operator is calculated explicitly in Appendix A. In what follows, a simplified spontaneous-emission pattern is assumed: fluorescence photons are emitted only along the x, y, and z axes. This modification will greatly simplify the numerical calculations required by the quantum treatment of the cooling process. Indeed it allows one to use a grid for the atomic momentum distribution with a step as large as the photon momentum $\hbar k$. This simplification is justified because the minimal rms atomic momenta are found to be several photon momenta $\hbar k$. For example, in 1D, the corresponding assumption introduced an error on rms momenta on the order of $0.2\hbar k$ [14]. The resulting relaxation operator is

$$\mathcal{L}_{\text{relax}}(\rho, k\vec{r}) = -2\{V(k\vec{r}), \rho\} + \frac{1}{8}\sum_{\epsilon=\pm}\sum_{m=x,y,z}\sum_{l\neq m} e^{-ik\epsilon r_l} B_m \rho B_m^{\dagger} e^{ik\epsilon r_l} \ . \tag{9}$$

It involves a sum over the polarization (along the $m = x, y$, or z axis) and the direction (backward $\varepsilon = -$ or forward $\varepsilon = +$ along the l axis) of the fluorescence photon. In (9) the following operators have been introduced:

$$\begin{aligned} B_x &= -\frac{1}{\sqrt{2}}\left(\mathcal{E}_+ - \frac{1}{3}\mathcal{E}_-\right)|+\rangle\langle+| \\ &\quad -\frac{1}{\sqrt{2}}\left(\mathcal{E}_- - \frac{1}{3}\mathcal{E}_+\right)|-\rangle\langle-|\,, \\ B_y &= \frac{1}{\sqrt{2}}\left(\mathcal{E}_+ + \frac{1}{3}\mathcal{E}_-\right)|+\rangle\langle+| \\ &\quad +\frac{1}{\sqrt{2}}\left(\mathcal{E}_- + \frac{1}{3}\mathcal{E}_+\right)|-\rangle\langle-|\,, \\ B_z &= \frac{\sqrt{2}}{3}\mathcal{E}_+|+\rangle\langle-| + \frac{\sqrt{2}}{3}\mathcal{E}_-|-\rangle\langle+|\,, \end{aligned} \tag{10}$$

where the $\sigma_\pm$ reduced components $\mathcal{E}_\pm$ of the laser electric field are given in (6).

A feature of the relaxation operator (9) that will be particularly useful in Sec. III is the absence of coupling between the ground-state populations $\langle\pm|\rho|\pm\rangle$ and the ground-state coherences $\langle\pm|\rho|\mp\rangle$. As shown in Appendix A, the same property is true when the exact spontaneous-emission pattern is considered, since the absence of coupling is due to the trace taken over atomic motion along the z axis.

We emphasize that, due to the factorization of δs_0 and Γs_0, the operators V and $\mathcal{L}_{\text{relax}}$ appearing in (4) and (8) depend on neither the intensity of the light nor its detuning from the atomic resonance. These operators are only functions of the geometry of the configuration which has been chosen. Note that this property relies on the procedure used for the elimination of the excited state. In particular, it requires that the contribution to laser cooling, known as Doppler cooling in semiclassical theory [15] and acting on a velocity scale $v = \Gamma/k$, can be neglected. Such a procedure is legitimate as long as one considers velocity distributions with a rms velocity $\bar{v}$ much smaller than the ones obtainable by Doppler cooling, i.e., $M\bar{v}^2 \ll \hbar\Gamma/2$.

B. Scaling laws

In a given geometry such as the one corresponding to the field (1), and for a $1/2 \leftrightarrow 3/2$ atomic transition, several physical parameters are required to characterize a given laser cooling situation. Concerning the atom, one needs to know the atomic mass M, the wavelength λ, and the natural width Γ. In addition, the atom-laser coupling is characterized by the Rabi frequency Ω and the detuning δ. Actually, it is possible to choose reduced units so that these five parameters are reduced to only two independent parameters. A possible choice is to take the reduced position $\vec{R}$ and momentum $\vec{P}$ operators and the reduced time scale τ given by

$$\vec{R} = k\vec{r}\,, \quad \vec{P} = \frac{\vec{p}}{\hbar k}\,, \quad \tau = \Gamma s_0 t. \tag{11}$$

The equation of motion (3) then becomes

$$\frac{d\rho}{d\tau} = 8i\frac{\Delta}{u_0}\left[\rho, \frac{P^2}{2} - \frac{u_0}{2}V(\vec{R})\right] + \mathcal{L}_{\text{relax}}(\rho, \vec{R})\,. \tag{12}$$

Since $\vec{P} = -i\partial_{\vec{R}}$, Eq. (12) involves the two dimensionless parameters:

$$u_0 = \frac{-4\hbar\delta s_0}{E_R}, \qquad \Delta = \frac{\delta}{\Gamma}\,, \tag{13}$$

where $E_R = \hbar^2k^2/2M$ stands for the recoil energy, i.e., the kinetic energy gained by an atom at rest after emission of a photon. The parameter u_0 gives the magnitude of the light shift of the atomic ground level, measured in units of the recoil energy E_R, and Δ is the detuning measured in units of linewidth. Note that this reduction of the problem to two independent parameters is useful not only for studying the steady state of the atom, but also transient regimes, spatial diffusion in the molasses, etc. Note also that if Doppler cooling had been kept, a third dimensionless parameter, such as $\epsilon = E_R/\hbar\Gamma$, would be required to characterize a given situation. The treatment presented here corresponds to the mathematical limit $\epsilon \to 0$, for given u_0 and Δ.

III. SEMICLASSICAL METHOD

Before going to the solution of the quantum equation of motion, we present in this section an approximate semiclassical approach, which has the advantage of being very close to the intuitive picture of Sisyphus cooling. Applying this method we shall be able to evaluate the effect of a truncation in the momentum space on various quantities calculated in the steady state. This is important information since such a truncation cannot be avoided in the quantum calculation, which requires an expansion of the atomic wave function or density matrix on a finite subset of the momentum basis.

A. Evolution of the Wigner distribution

Our goal here is to connect the quantum equations of motion (3) to the evolution of classical particles, with two possible internal states, moving in the bipotential $U_\pm$ and jumping at random between these two states. This is reached in two steps. First, we write the master equation (3) using the Wigner representation $W(\vec{r}, \vec{p}, t)$ of the atomic density matrix $\rho(t)$. We then perform some simplifications on the equation in order to be able to associate to this equation a stochastic classical process, which is studied using a standard Monte Carlo method.

The Wigner transform of the atomic density matrix $\rho(t)$ is defined as

$$\begin{aligned} W(\vec{r}, \vec{p}, t) = \frac{1}{(2\pi\hbar)^2}\int d^2u \left\langle \vec{r} + \frac{\vec{u}}{2}\left|\rho(t)\right|\vec{r} - \frac{\vec{u}}{2}\right\rangle \\ \times \exp(-i\vec{p}\cdot\vec{u}/\hbar)\,. \end{aligned} \tag{14}$$

For a given phase space point $(\vec{r},\vec{p})$, W is a 2×2 matrix acting in the Hilbert space associated with the internal atomic ground state.

As we have seen above, the Hamiltonian H is diagonal in the basis g_+, g_- and the relaxation term (9) does not couple diagonal and nondiagonal matrix elements in this basis. Therefore we will need in the following only the evolution of the two quantities $\Pi_\epsilon(\vec{r},\vec{p},t) = \langle g_\epsilon|W(\vec{r},\vec{p},t)|g_\epsilon\rangle$ with $\epsilon = \pm$. The two quantities $\Pi_+(\vec{r},\vec{p},t)$ and $\Pi_-(\vec{r},\vec{p},t)$ give the quasiprobability density in phase space for finding the atom in states g_+ and g_-, at position $\vec{r}$, and with momentum $\vec{p}$.

The derivation of the equations of motion of $\Pi_\pm$ is lengthy, but straightforward. These equations of motion take the form of two integro-differential equations, where $\Pi_\epsilon(\vec{r},\vec{p},t)$ is coupled to $\Pi_{\epsilon'}(\vec{r},\vec{p}',t)$, with $|\vec{p}-\vec{p}'| < 2\hbar k$. Since we expect the steady-state momentum distributions to have an extension $\bar{p}$ in momentum space of a few $\hbar k$, we now expand these equations of motion in powers of $\hbar k/\bar{p}$ to second order. The resulting equations are no longer equivalent to the master equation (3) and some specific quantum features of the atomic motion in the optical potential wells may be lost. We obtain

$$\left(\partial_t + \frac{\vec{p}}{M}\cdot\partial_{\vec{r}} - \partial_{\vec{r}}U_+(\vec{r})\cdot\partial_{\vec{p}}\right)\Pi_+ = -\gamma_{+-}\Pi_+ + \gamma_{-+}\Pi_- - \sum_{i=x,y}\partial_{p_i}(F^i_{++}\Pi_+ + F^i_{-+}\Pi_-) + \sum_{i,j=x,y}\partial_{p_i}\partial_{p_j}(D^{ij}_{++}\Pi_+ + D^{ij}_{-+}\Pi_-) \tag{15}$$

and a similar equation for Π_-. In (15) the potential

$$U_+ = 4\hbar\delta s_0 V_+ \tag{16}$$

is the light shift of the $|+\rangle$ ground-state sublevel and γ_{+-} and γ_{-+} are the optical pumping rates from $|\pm\rangle$ to $|\mp\rangle$ internal sublevels. As expected, these rates scale with the saturation parameter s_0 and are proportional to the intensities of the $\sigma_\mp$ components of the laser electric field given in Eq. (6):

$$\gamma_{+-} = \frac{1}{9}\Gamma s_0|\mathcal{E}_-|^2, \quad \gamma_{-+} = \frac{1}{9}\Gamma s_0|\mathcal{E}_+|^2 . \tag{17}$$

Equation (15) is the result of a systematic expansion of the master equation, but contrary to the traditional semiclassical treatment, we have kept the internal states $\pm$. The first line accounts for Sisyphus cooling in the way it was described in the Introduction, but now the atomic motion is governed by additional force and diffusion-type terms in the second and third lines.

We may derive from the first line of Eq. (15) an estimate of the cooling efficiency for high-energy atoms. Assuming that $\Pi_+(\vec{r},\vec{p},t) = \Pi_-(\vec{r},\vec{p},t) = \Pi(\vec{r},\vec{p},t)/2$ and that these functions do not vary with position on the wavelength scale, we get for the total, the kinetic, and the potential energy

$$\frac{d}{dt}\langle E\rangle = \frac{1}{2}\langle (U_- - U_+)(\gamma_{+-}-\gamma_{-+})\rangle_{\vec{r}} = \frac{8}{27}\hbar\delta s_0\Gamma s_0\sin^2\alpha , \tag{18}$$

which is negative for $\delta < 0$ and $\sin\alpha \neq 0$. This cooling rate corresponds as expected to a fraction of a light shift $\hbar\delta s_0$ per optical pumping time $(\Gamma s_0)^{-1}$. The validity of this result is limited by the fact that high-energy atoms do not necessarily have a uniform distribution in space. As we see below, the classical Monte Carlo calculation gives evidence of substantial channeling of atoms along preferred trajectories in the x-y plane. This implies a reduction of the cooling rate, as can be understood by introducing weighted averages in the derivation of $d\langle E\rangle/dt$ (see discussion in Sec. III E).

The forces $\vec{F}_{++}$ and $\vec{F}_{-+}$ in Eq. (15) can be written, setting $c_x = \cos kx, s_x = \sin kx, c_y = \cos ky, s_y = \sin ky$,

$$\vec{F}_{++} = \frac{8}{9}\hbar k\Gamma s_0\cos\alpha(-s_xc_y, c_xs_y) = 4\vec{F}_{-+} . \tag{19}$$

The existence of the $\vec{F}_{-+}$ component implies a momentum change of $\gamma_{-+}^{-1}\vec{F}_{-+}$ associated with each jump of the atom from the $-$ to the $+$ sublevel. Both $\vec{F}_{++}$ and $\vec{F}_{-+}$ correspond to the local mean radiation pressure and have a vortex-type structure. A similar vortex force has been studied in [9] in a different 2D laser configuration for a two-level atom and it has been related for that configuration to the vortex structure of the Poynting vector $\vec{S}$. In our laser configuration, the local Poynting vector $\vec{S}$ vanishes everywhere, but for a given sublevel of $J_g = 1/2$ the radiation pressure is not proportional to $\vec{S}$. This is due to the different Clebsch-Gordan coefficients entering in the coupling of the ground-state sublevel $|+\rangle$ (or $|-\rangle$) to the σ_+ and σ_- components of the laser electric field. We note, however, that the vortex forces vanish when $\alpha = \pi/2$.

The "momentum diffusion tensors" D_{++} and D_{-+} in Eq. (15) are given by

$$D_{++} = \begin{pmatrix} D^{xx}_{++} & D^{xy}_{++} \\ D^{yx}_{++} & D^{yy}_{++}\end{pmatrix} = \frac{\hbar^2k^2\Gamma s_0}{18}\begin{pmatrix} 11+5c_xc_y\sin\alpha - 8c_x^2 + c_y^2 & 7s_xs_y\sin\alpha \\ 7s_xs_y\sin\alpha & 11+5c_xc_y\sin\alpha + c_x^2 - 8c_y^2\end{pmatrix} , \tag{20}$$

$$D_{-+} = \begin{pmatrix} D^{xx}_{-+} & D^{xy}_{-+} \\ D^{yx}_{-+} & D^{yy}_{-+} \end{pmatrix}$$

$$= \frac{\hbar^2 k^2 \Gamma s_0}{18} \begin{pmatrix} 1 + 3c_x c_y \sin\alpha + c_x^2 + c_y^2 & s_x s_y \sin\alpha \\ s_x s_y \sin\alpha & 1 + 3c_x c_y \sin\alpha + c_x^2 + c_y^2 \end{pmatrix} . \quad (21)$$

The momentum diffusion tensors D_{--} and D_{+-} to use in the equation of motion for Π_- are similar to (15) and are obtained by replacing y by $y - \lambda/2$ in (20) and (21).

B. Classical stochastic equations

We restrict ourselves to the particular case $\alpha = \pi/2$, where the most efficient Sisyphus cooling is expected, according to (18), and where there are no vortex forces. Therefore the second line of (15) vanishes. (Quantum calculations of the kind described in Sec. V have been performed also for $\alpha = \pi/4$ [16] and they show indeed that the width of the atomic momentum distribution is increased compared to the case $\alpha = \pi/2$.)

The physical interpretation of the first line of (15) is clear. It corresponds to the classical motion of an assembly of particles with mass M, with two internal states $+$ and $-$, evolving in the potential $U_\pm$, and randomly jumping among $+$ and $-$ with the rates γ_{+-} and γ_{-+}.

The third line of (15) describes the momentum diffusion associated with the relaxation part of the master equation. Contrary to the first line, it is not possible to give a simple interpretation of these terms in reference to a classical process. For instance, the "diffusion tensor" D_{++} has in some locations (e.g., $x = 0$, $y = \lambda/2$) negative eigenvalues, while one expects that a classical diffusion tensor is always positive. Also the diffusion tensor D_{-+} can be nonzero in a place where $\gamma_{-+} = 0$, while one would expect $D_{-+} \sim q^2 \gamma_{-+}$ in a classical stochastic process where the particle randomly jumps from $-$ to $+$ while receiving a random kick q. An equivalent problem occurs for a two-level atom at the node of a standing wave and it has been studied in detail in [12].

The negative components of the diffusion tensors are reminiscent of the quantum nature of the atomic motion. Here we briefly summarize an explanation for these anomalous diffusion terms. Consider an assembly of classical particles at rest at the location $x = 0$, $y = \lambda/2$ where the light is purely σ_-. If these atoms are all in the ground state sublevel $|+\rangle$, they will experience a diffusive heating due to the absorption and subsequent spontaneous emission of σ_- light. This contributes to the D_{++} diffusion tensor and is illustrated in Fig. 1(a). The optical pumping process via emission of light, linearly polarized along the z axis, contributes to D_{+-} as indicated in Fig. 1(b). Now, quantum mechanics forces us to impose a finite position and momentum width to the atomic motion. The quantum analog of the particles at rest in the potential well is the oscillator ground-state wave function. The γ_{+-} rate causes a depletion of the wave function and this depletion is maximum at ($x = 0$, $y = \lambda/2$), where γ_{+-} is maximum. With a quadratic falloff of γ_{+-}, we find to first order in time that the position wave function remains Gaussian, but with an increased width. The corresponding momentum wave function is therefore getting narrower, which indicates a negative contribution to the momentum diffusion coefficient. This negative contribution to D_{++} even exceeds the positive terms, accounted for above, causing the total D_{++} to be negative in this particular point. This quantum correction of course exists everywhere and it also has a negative sign in the global minima, e.g., at ($x = 0$, $y = 0$), without, however, causing the total D_{++} to be negative.

We cannot mimic these negative terms by a classical stochastic process. Therefore, in order to perform a classical Monte Carlo analysis of the problem, we have replaced (15) by a slightly different equation of motion. Since we expect in steady state a strong spatial localization around ($x = 0$, $y = 0$) (modulo the spatial periods of U_+) for not too fast particles ($|\vec{p}| \sim \bar{p}$) in state $|+\rangle$, we replace the position-dependent tensor D_{++} by its value $\bar{D}_{++}$ in $(0,0)$. We also approximate the diffusion tensor D_{-+} by a position-dependent scalar tensor $\bar{D}_{-+}$ proportional to the transition rate γ_{-+} from $|-\rangle$ to $|+\rangle$. Since the feeding of Π_+ involves hot particles in the $|-\rangle$ sublevel, one can consider that these particles are almost uniformly distributed in position space. We therefore choose the normalization factor in $\bar{D}_{-+}$ in order to have the same spatial average for $\bar{D}_{-+}$ and D_{-+}.

We finally get the approximate equation for $\alpha = \pi/2$:

$$\left(\partial_t + \frac{\vec{p}}{M} \cdot \partial_{\vec{r}} - \partial_{\vec{r}} U_+(\vec{r}) \cdot \partial_{\vec{p}}\right) \Pi_+ = -\gamma_{+-}\Pi_+ + \gamma_{-+}\Pi_- + (\partial^2_{p_x} + \partial^2_{p_y})(\bar{D}_{++}\Pi_+ + \bar{D}_{-+}\Pi_-) \quad (22)$$

FIG. 1. The absorption of a σ_- polarized photon and emission processes involved in the diffusion terms. In (a) the process contributing to D_{++} is shown and in (b) we show the contribution to D_{+-}.

with

$$\bar{D}_{++} = \frac{1}{2}\hbar^2 k^2 \Gamma s_0 \ , \tag{23}$$

$$\bar{D}_{-+} = \frac{1}{2}\hbar^2 k^2 \gamma_{-+} = \frac{1}{9}\hbar^2 k^2 \Gamma s_0 (c_x + c_y)^2 \ . \tag{24}$$

The classical stochastic process associated with (22) is now very simple and it can be studied with a Monte Carlo analysis by evolving a set of N particles with two internal states + and −. The jump rates between these two states are given by γ_{+-} and γ_{-+} and each jump is accompanied by random kicks with a rms value $\hbar k$ along each direction x and y to simulate the diffusion associated with $\bar{D}_{-+}$ and $\bar{D}_{+-}$. Between two jumps, the particles evolve under the action of the potential U_+ or U_- and also receive random kicks to simulate the effect of $\bar{D}_{++}$ or $\bar{D}_{--}$.

From the Monte Carlo solution of (22), we can calculate the phase space distribution $\Pi_\epsilon^{(MC)}(\vec{r},\vec{p},t)$. We can also use the classical simulation to estimate the population $\pi_{0,\epsilon}$ of a given quantum state $\phi_{0,\epsilon}(\vec{r})$. We introduce the Wigner function $W_0(\vec{r},\vec{p})$ associated with $\phi_{0,\epsilon}$ (14) and we obtain

$$\begin{aligned}\pi_{0,\epsilon}(t) &= \mathrm{Tr}\,(\rho|\phi_{0,\epsilon}\rangle\langle\phi_{0,\epsilon}|) \\ &= \int d^2\vec{r}\int d^2\vec{p}\,\Pi_\epsilon(\vec{r},\vec{p})W_0(\vec{r},\vec{p}) \\ &\simeq \frac{1}{N}\sum_{i=1}^{N}\delta_{\epsilon,\epsilon_i}W_0(\vec{r}_i,\vec{p}_i) \ ,\end{aligned} \tag{25}$$

where $\vec{r}_i(t)$, $\vec{p}_i(t)$, and $\epsilon_i(t)$ denote the position, momentum, and internal state of the particle i at time t.

C. Results of the semiclassical calculation

We have performed a Monte Carlo evolution for a set of $N = 4000$ particles moving according to (22), for various values of u_0 and Δ. All the particles start in the internal level +, in the ground state of the optical potential U_+. In the range of values of u_0 considered in this paper ($u_0 < 1000$), we have observed that a time evolution of $2000(\Gamma s_0)^{-1}$ is usually large enough to ensure that the steady state is reached. An example of such an evolution, showing $\langle p^2\rangle$ as a function of time, is given in Fig. 2 for $u_0 = 400$ and $\Delta = -10$. In what follows, we have averaged the various calculated quantities over the time interval $2000 \le \Gamma s_0 t \le 4000$, in order to decrease the statistical uncertainty.

In addition to the rms momentum, we calculate in steady state three other quantities: (i) the population π_0 of the ground state of the motion in $U_\pm(\vec{r})$ as indicated in Sec. III B, (ii) the half width $p_{e,x}$ at relative height $e^{-1/2}$ of the momentum distribution along $\vec{e}_x$, i.e., of $\int dp_y \Pi(p_x,p_y)$, and (iii) the corresponding half width $p_{e,\xi}$ of the momentum distribution along $\vec{e}_\xi = (\vec{e}_x + \vec{e}_y)/\sqrt{2}$. For a Gaussian distribution, the last two quantities coincide with the rms momentum along a given axis, so that one expects, for such a Gaussian distribution, $\langle p^2\rangle = 2p_{e,x}^2 = 2p_{e,\xi}^2$. In experimental investigations, the half width of the momentum distribution along one specific direction may be a more relevant parameter than $\langle p^2\rangle$.

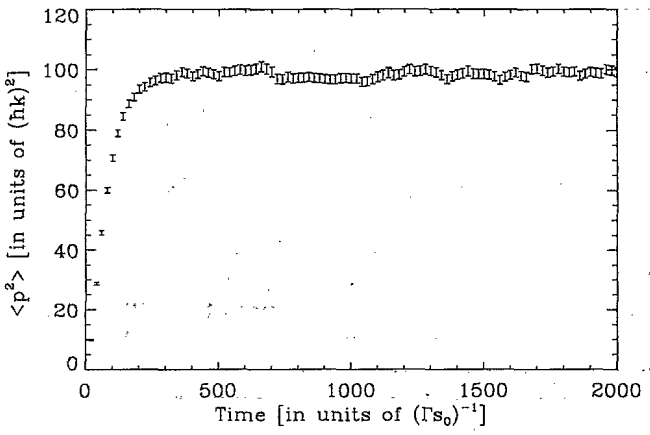

FIG. 2. The temporal evolution of $\langle p^2\rangle$ in the semiclassical Monte Carlo evolution of 4000 atoms, for parameters $u_0 = 400$ and $\Delta = -10$.

The variations of $\langle p^2\rangle$, $2p_{e,x}^2$, $2p_{e,\xi}^2$, and π_0 as functions of u_0 are plotted in Figs. 3(a) and 3(b). The detuning chosen for this figure is $\Delta = -10$, but we have varied Δ between −5 and −30 without any qualitative change.

We see in Fig. 3(a) that $\langle p^2\rangle$ is only defined for relatively large values of u_0. The minimum $\sqrt{\langle \vec{p}^2\rangle} = 9.0\hbar k$, corresponding to a rms momentum of $6.4\hbar k$ per axis, is found for $u_0 = 300$. Below $u_0 = 200$, this quantity does not reach a steady state, but increases indefinitely with time, as we have checked in using the much longer interaction time Γst =20 000, instead of $\Gamma st = 4000$. This divergence is due to escape channels along the axes $x = \pm y[\lambda]$, as discussed in further detail in Sec. III E. The existence of such escape channels has been predicted independently by Dum and Zoller [17]. This channeling effect is most prominent for small u_0. For instance, Fig. 4 shows two momentum distributions obtained after an evolution during $2000(\Gamma s_0)^{-1}$, for (a) $u_0 = 100$ and (b) $u_0 = 400$. For $u_0 = 100$, many particles are found with a high momentum such that $|p_x| \simeq |p_y|$. For $u_0 = 400$, on the contrary, the distribution does not show any evidence of escape channels.

The variations of $p_{e,x}^2$ and $p_{e,\xi}^2$ shown in Fig. 3(a) are similar to those of $\langle p^2\rangle$, but the corresponding minimum values of $p_{e,x}$, $3.9\hbar k$, and $p_{e,\xi}$, $2.2\hbar k$, are reached for much smaller values of the light shifts, $u_0 \sim 40$ and $u_0 \sim 20$, respectively. The fact that $p_{e,\xi}$ can become much smaller than $p_{e,x}$ at low values of u_0 is again a consequence of the channeling of atoms in momentum space along the lines $p_x = \pm p_y$.

As is commonly done to present experimental data, we can deduce from our results for $\langle p^2\rangle$ and $p_{e,x}^2$, $p_{e,\xi}^2$, a "temperature." As is apparent in Fig. 3(a) for large u_0, this temperature is found to vary linearly with u_0. By a linear fit for $u_0 > 400$, we have found the approximate laws

$$k_B T_{\langle p^2 \rangle} = \frac{\langle p^2 \rangle}{2M} \simeq (0.19u_0 + 21)E_R \ , \tag{26}$$

$$k_B T_{p_{e,x}} = \frac{p_{e,x}^2}{M} \simeq (0.34u_0 + 19)E_R \ , \tag{27}$$

$$k_B T_{p_{e,\xi}} = \frac{p_{e,\xi}^2}{M} \simeq (0.24u_0 + 15)E_R \ . \tag{28}$$

The variation of π_0 as a function of u_0 is reproduced in Fig. 3(b) for $\Delta = -10$. As for $p_{e,x}$ and $p_{e,\xi}$, a steady state can be reached even for low values of u_0. The maximal value $\pi_0 = 0.049$ is obtained for $u_0 \simeq 80$. We can also use π_0 to define a temperature T_{π_0}. We introduce the 2D harmonic oscillator corresponding to the harmonic part of the potential U_+ around $x = y = 0$, i.e., with an oscillation frequency $\Omega_{\rm osc}$ given by

$$M\Omega_{\rm osc}^2 = \frac{1}{2}(\partial_x^2 U_+ + \partial_y^2 U_+)(0,0) = -4\hbar k^2 \delta s_0 \ , \tag{29}$$

so that $\hbar\Omega_{\rm osc} = \sqrt{2u_0}E_R$. The temperature T_{π_0} is such that the population in the ground state of the previous 2D harmonic oscillator is π_0 in thermal equilibrium. For large values of u_0, the approximate law follows:

$$k_B T_{\pi_0} = -\frac{\hbar\Omega_{\rm osc}}{\ln(1-\sqrt{\pi_0})} \simeq \frac{\hbar\Omega_{\rm osc}}{\sqrt{\pi_0}} \simeq (0.39u_0 + 31)E_R \ , \tag{30}$$

which gives a temperature larger than (26)–(28). The behavior of π_0 as a function of u_0 corresponding to the law (30) is plotted as a dashed line in Fig. 3(b). This shows that (30) is a good approximation even for low values of u_0.

The discrepancy between the four temperatures that we have deduced from the phase space distribution is a good illustration of the non-Gaussian character of this distribution. For instance, the fact that the rms kinetic energy $\langle p^2 \rangle/2M$ is smaller than $p_{e,x}^2/M$ and $p_{e,\xi}^2/M$, for $u_0 > 300$, indicates that the momentum distribution is less extended than a Gaussian distribution. This discrepancy should also be considered as a warning against characterizing a given laser cooled steady-state distribution by a single temperature parameter.

Another piece of information that we have extracted from these Monte Carlo evolutions for different u_0 and Δ is a typical time constant for the cooling process. We

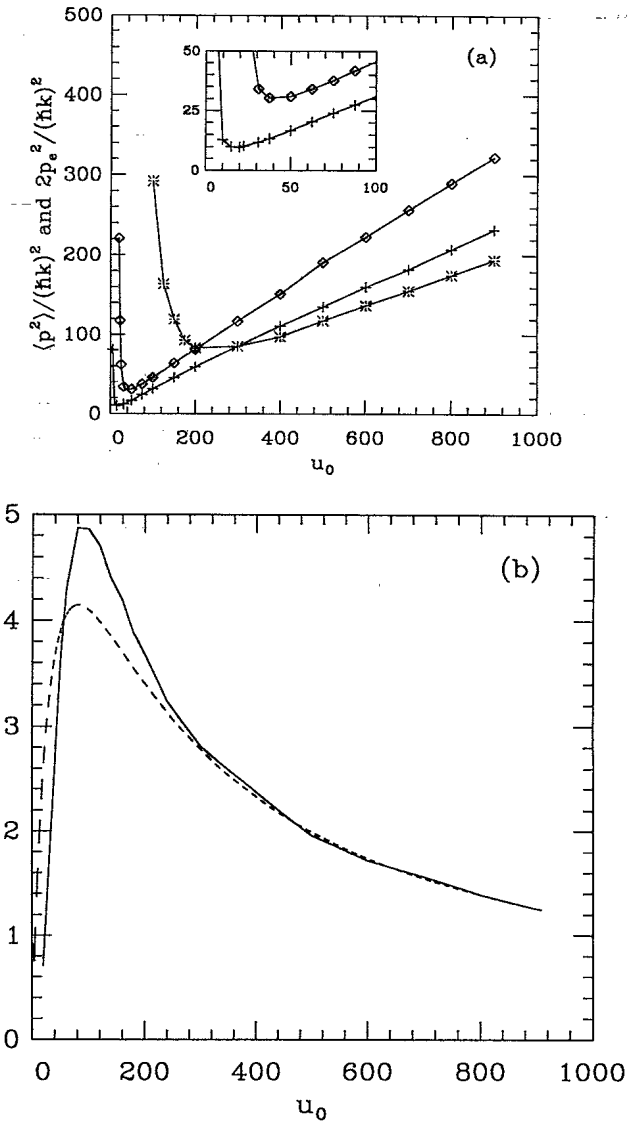

FIG. 3. The results of the semiclassical calculations for (a) $\langle p^2 \rangle$ (*), $2p_{e,x}^2$ ($\diamond$), and $2p_{e,\xi}^2$ (+), where $p_{e,x}$ and $p_{e,\xi}$ are the half widths at the relative height $e^{-1/2}$ of the momentum distributions along x and ξ and (b) the population of the ground state of the atomic motion π_0 (solid line). The dashed line gives the population deduced from the linear fit of the "temperature" T_{π_0} with u_0 presented in Sec. III C. The results were calculated with a detuning of $\Delta = -10$ and evolution of 4000 atoms in $4000/(\Gamma s_0)$.

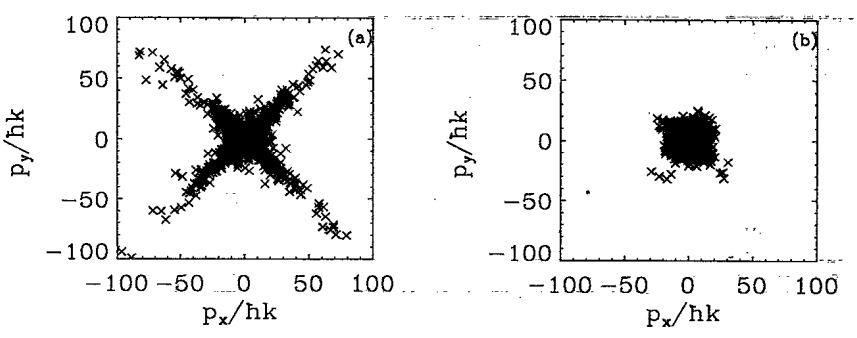

FIG. 4. Two momentum distributions obtained by the semiclassical calculations. The channeling of the atoms along the lines $p_x = \pm p_y$ is clear for the low potential depth in (a), $u_0 = 100$, whereas for the larger value $u_0 = 400$, shown in (b), the atoms do not escape. Both calculations were performed with a total number of atoms of 4000 over a time interval of $2000(\Gamma s_0)^{-1}$.

have fitted by an exponential law the long time part of the temporal behavior of $\langle p^2 \rangle$ (such as the one shown in Fig. 2), where this quantity differs by less than 30% from its steady-state value. The same type of fit was performed for $\pi_0(t)$ on the time interval where π_0 differs by less than a factor 3 from its final value. The results of the two fits are nearly equivalent and lead, for large u_0 [$u_0 > 400$, as in (26) and (30)], to a time constant on the order of $|\delta|M/\Gamma\hbar k^2 = (\Gamma s_0)^{-1} u_0/8$.

D. Truncation effects

In a classical Monte Carlo evolution, the momentum of a given atom can take arbitrarily large values; this is, for instance, reflected in the existence of escape channels along $|p_x| = |p_y|$, causing a divergence of the time evolution of $\langle p^2 \rangle$ for $u_0 < 200$. On the contrary, in the quantum calculations based either on the evolution of the density matrix or on the secular approach, one uses a finite grid for the momentum distribution, requiring a truncation in momentum space. It is therefore interesting to use the classical Monte Carlo evolution to study the consequences of such a truncation. This can be done simply by adding to the equations of motion (22) the condition that the momentum of the particle has to remain lower than a given bound. If the momentum becomes greater than this bound, the particle does not contribute to the average anymore. This simulates absorbing boundary conditions for the evolution of the atomic density matrix.

The boundary is chosen to mimic the grid used for the quantum calculation. It is defined by the maximal momentum of the atoms along the rotated axes $(\vec{e}_x \pm \vec{e}_y)/\sqrt{2}$:

$$\frac{1}{\sqrt{2}}|p_x \pm p_y| \leq n_{\max}\sqrt{2}\hbar k \quad \text{with} \quad n_{\max} = 15 \, . \qquad (31)$$

The value of the cutoff parameter $n_{\max} = 15$ is the one used for the quantum calculations in Secs. IV and V. For such a low value of $n_{\max}$, the typical evolution time necessary for the system to reach a steady state is much shorter than in the absence of truncation. We have assumed that it is less than $500(\Gamma s_0)^{-1}$ and we have performed an average over the time interval $500 \leq \Gamma s_0 t \leq 1000$. In order to improve the statistics, an initial number of 8000 atoms is considered. The results for the various quantities of Sec. III C obtained with the truncation are plotted in Fig. 5(a) with the same symbols as in Fig. 3(a). In Fig. 5(b), the dotted line corresponds to the values of π_0 calculated without truncation and already given in Fig. 3(b). The strongest modification due to the truncation occurs for $\langle p^2 \rangle$, which is now minimal for $u_0 = 100$, instead of $u_0 = 300$ in the absence of truncation. This is a consequence of the fact that the escape channels are now closed. The modifications on the half-widths and on the population of the ground state π_0 are much less important, at least for the values of u_0 considered in Fig. 5 ($u_0 < 400$). Consequently, these last three quantities can be evaluated in a reliable way in a quantum calculation having the boundary condition (31).

E. Channeling of the atoms

The classical Monte Carlo simulations give evidence of a threshold on the potential depth for the cooling to be effective. When u_0 is decreased below a value ~ 200, the mean atomic kinetic energy $\langle p^2 \rangle/(2M)$ no longer reaches a steady-state value, but is increasing linearly with time.[1] This increase of $\langle p^2 \rangle$ does not imply a general escape of the atoms toward high momenta since the population π_0 of the ground state of the optical potential wells still reaches a nonzero steady-state value. It is due to a channeling of a finite fraction of the atoms along the rotated lines:

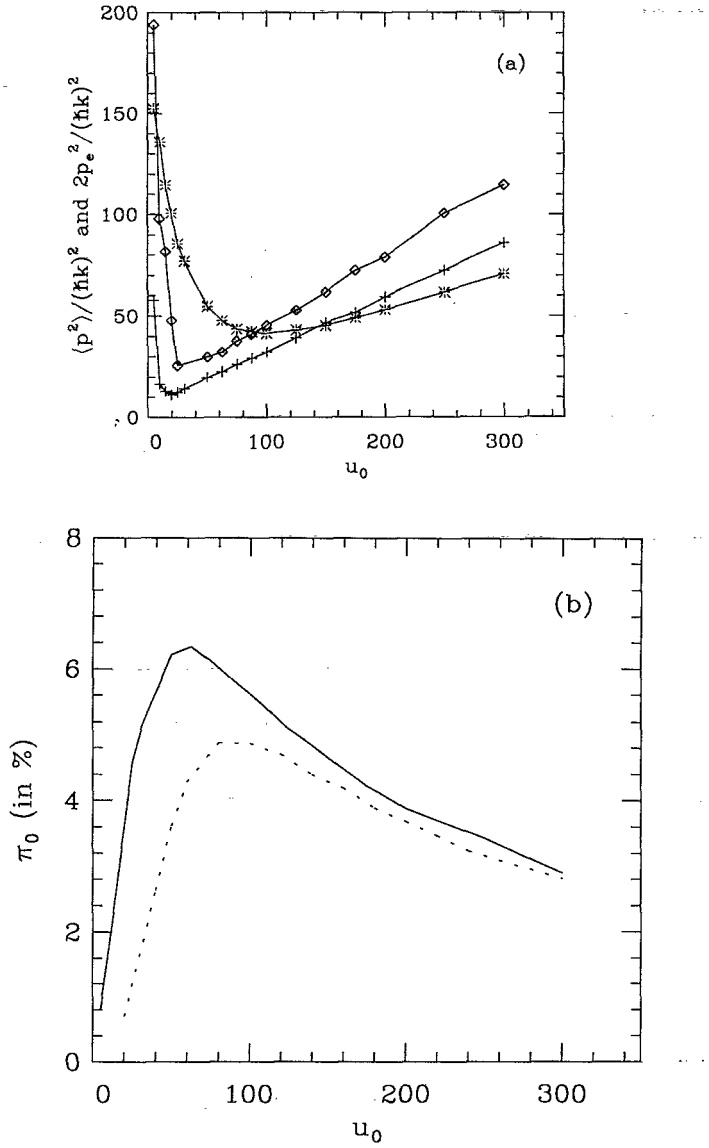

FIG. 5. The results of the semiclassical calculations performed with a truncation in momentum space corresponding to a cutoff parameter $n_{\max} = 15$ [see Eq. (31)], for (a) $\langle p^2 \rangle$ (*), $2p_{e,x}^2$ (◇), and $2p_{e,\xi}^2$ (+) and (b) π_0 (solid line) as functions of u_0. The dotted line corresponds to the predictions of Fig. 3(b) (obtained without truncation). The results were calculated with a detuning of $\Delta = -10$ and evolution of an initial number of 8000 atoms in $1000/(\Gamma s_0)$.

$$\vec{e}_\xi = \frac{1}{\sqrt{2}}(\vec{e}_x + \vec{e}_y) , \tag{32}$$

$$\vec{e}_\eta = \frac{1}{\sqrt{2}}(\vec{e}_x - \vec{e}_y) \tag{33}$$

in momentum space, where they reach very high velocities (see Fig. 4).

In order to get some understanding of this channeling, we consider the evolution of a jet of atoms with a large velocity along $\vec{e}_\eta$. Since we expect the longitudinal velocity v_η to evolve on a time scale longer than the one for the transverse velocity v_ξ, we consider v_η to have the fixed value v_0, but we keep v_ξ as a dynamical variable. As shown in Appendix B, we are now left with a 1D problem, with the following optical potential wells and optical pumping rates, deduced from an average of (16) and (17) over η:

$$\langle \gamma_{\pm\mp} \rangle_\eta = \frac{2}{9}\Gamma s_0 (1 \mp \cos \tilde{k}\xi) , \tag{34}$$

$$\langle U_\pm \rangle_\eta = \frac{2}{3}\hbar\delta s_0 (2 \pm \cos \tilde{k}\xi) , \tag{35}$$

where $\tilde{k} = k\sqrt{2}$. The spatial modulation in (34) and (35) leads to a Sisyphus effect along the ξ axis, in a way similar to the 1D lin⊥lin standard model on the $J_g = 1/2 \rightarrow J_e = 3/2$ transition (lin⊥lin is an abbreviation for a setup of two counterpropagating laser beams with orthogonal linear polarizations).

This leads to the following qualitative understanding of the channeling along η. Consider a value of u_0 leading to efficient transverse Sisyphus cooling along the ξ axis so that the atoms of the jet keep their momentum quasiparallel to the η axis. The atoms also accumulate in position space at the bottom of the potential wells (35), i.e., in the vicinity of the lines $\tilde{k}\xi = 0\ [2\pi]$ for the $|+\rangle$ sublevel and the lines $\tilde{k}\xi = \pi\ [2\pi]$ for the $|-\rangle$ sublevel. Along these lines, the laser electric field is purely circularly polarized and there is no longitudinal Sisyphus effect. The efficiency of the longitudinal cooling (i.e., along the η axis) is therefore decreased by the transverse spatial localization of the atoms. This suggests that the threshold $u_0^\parallel$ for longitudinal cooling, of p_η, may be larger than the corresponding threshold $u_0^\perp$ for the transverse cooling. For values of u_0 between $u_0^\perp$ and $u_0^\parallel$, atoms are captured and channeled by the transverse cooling, but their motion along η is heated.

This discussion is supported by the quantitative treatment of Appendix B, where we derive the explicit values of the thresholds for the existence of a finite momentum variance. We obtain $u_0^\perp \simeq 100$ and $u_0^\parallel \simeq 5u_0^\perp/3 \simeq 165$.

We can extend the present discussion to the search for directions of channeling other than the rotated axes ξ and η. A first condition for the direction $\vec{n}$ to be an escape channel is that the optical potential wells $U_\pm$ averaged along $\vec{n}$ are spatially modulated transversally to $\vec{n}$. The only possible directions, apart from ξ and η, are found to be the laser axes x and y. These axes, however, do not obey the second condition, which is a modulation of the averaged optical pumping rates leading to Sisyphus cooling. The averaged rates $\langle \gamma_+ \rangle_y$ and $\langle \gamma_- \rangle_y$ are found to have exactly the same spatial dependence in x, so that no cooling along x can occur. This result can be stated in the more intuitive way: after averaging along y, the action of the laser standing wave along y becomes trivial, and one is left essentially with a 1D lin∥lin configuration along x, with no sub-Doppler cooling.

IV. INTEGRATION OF THE QUANTUM MASTER EQUATION

In this section we describe how to perform a numerical integration of the full quantum master equation (3) for the atomic density matrix, with the simplified relaxation operator (9) derived in Appendix A. Such a numerical integration requires fewer approximations than the other treatments used in this paper. It is used as a test of the classical Monte Carlo simulation (in Sec. VI) and of the secular approximation (in Sec. V).

Since the number of components of the atomic density matrix ρ scales as $(p_{\max}/\hbar k)^4$, where $p_{\max}$ is the radius of truncation in momentum space, this calculation is limited to not too large values of $p_{\max}/\hbar k$. Even so, the size of ρ would make a derivation of the steady-state density matrix by a direct inversion of the master equation technically difficult. We therefore perform a temporal evolution of the density matrix, until the steady state is reached. It is also easy in this way to use the sparse character of the master equation in momentum space.

In the numerical treatment of this section, the use of symmetries of the laser configuration leads to a substantial reduction of the size of the evolved objects. In the absence of laser light, only spontaneous processes occur and the corresponding evolution of the atomic density matrix is invariant under any translation in real space and under any reflection or rotation acting simultaneously on internal and external variables. These symmetries are partially broken by the laser field and one is left with a discrete group of symmetry operators acting in the atomic Hilbert space such that

$$S\mathcal{L}[\rho]S^\dagger = \mathcal{L}[S\rho S^\dagger] , \tag{36}$$

where the Liouvillian operator $\mathcal{L}$ is defined in Eq. (3). The translational symmetry of the laser-field configuration leads to a natural discretization of the problem discussed in Sec. IV A below. In Sec. IV B we show how reflection symmetries and a combination of a translation and a change of internal state may be applied to reduce the numerical problem. The practical implementation, i.e., the algorithm of integration and the choice of the time increment dt in the temporal evolution, are given in Sec. IV C.

[1] In a more exact treatment, including Doppler cooling, this increase stops when the mean kinetic energy reaches the Doppler limit proportional to $\hbar|\delta|$ for $|\delta| \gg \Gamma$.

A. Spatial translation symmetries and discretization of the problem

Consider the unitary operators $T(\vec{a})$ representing the spatial translations:

$$T(\vec{a}) = \exp(-i\vec{p}\cdot\vec{a}/\hbar) \ . \tag{37}$$

In order for $T(\vec{a})$ to generate a symmetry in the sense of Eq. (36), it is sufficient that the laser electric field (1) is preserved in the following way:

$$T(\vec{a})\vec{E}(\vec{r},t)T(\vec{a})^{\dagger} = \pm\vec{E}(\vec{r},t) \ . \tag{38}$$

The minus sign is allowed in Eq. (38) since the coefficients of the master equation have a quadratic dependence in $\vec{E}$. The largest translational symmetry group for the present field configuration is found to be generated by $T(\tilde{\lambda}\vec{e}_\xi)$ and $T(\tilde{\lambda}\vec{e}_\eta)$, where $\vec{e}_\xi$ and $\vec{e}_\eta$ are the unit vectors (32) and (33) and the rescaled wavelength $\tilde{\lambda} = \lambda/\sqrt{2}$ has been introduced. $T(\tilde{\lambda}\vec{e}_\xi)$ corresponds simply to a translation of $\lambda/2$ along each laser axis, which changes the sign of each of the standing waves along x and y.

The invariance by $T(\tilde{\lambda}\vec{e}_\xi)$ and $T(\tilde{\lambda}\vec{e}_\eta)$ corresponds in real space to a square lattice structure of $\vec{E}(\vec{r},t)$ along the rotated axes u and v. It is convenient to introduce also the reciprocal lattice $\{\vec{K}\}$ given by

$$\vec{K} = \tilde{k}(n_\xi\vec{e}_\xi + n_\eta\vec{e}_\eta) \qquad n_\xi, n_\eta \text{ integers} \ , \tag{39}$$

where the rescaled wave vector is $\tilde{k} = 2\pi/\tilde{\lambda} = k\sqrt{2}$. We note that the single photon wave vectors $\vec{k}_{x/y} = k\vec{e}_{x/y}$ do not belong to the reciprocal lattice, contrarily to the linear combinations $\vec{k}_x \pm \vec{k}_y$, $2\vec{k}_x$, $2\vec{k}_y$. Our choice for a unit cell of the reciprocal lattice (the so-called first Brillouin zone) is sketched in Fig. 6, together with a few reciprocal vectors $\vec{K}$. This unit cell can be described analytically by

$$-\frac{1}{2}\tilde{k} \le q_\xi, q_\eta < \frac{1}{2}\tilde{k} \ . \tag{40}$$

It amounts to writing in a unique way any atomic momentum $\vec{p}$ as

$$\vec{p} = \hbar(\vec{q} + \vec{K}) \ , \tag{41}$$

where $\vec{q}$ is in the first Brillouin zone and $\vec{K}$ is a vector of the reciprocal lattice. The so-called Bloch vector $\vec{q}$ determines the way the plane atomic wave $|\vec{p}\rangle$ transforms under $T(\vec{a})$:

$$T(\vec{a})|\vec{p}\rangle = e^{-i\vec{q}\cdot\vec{a}}|\vec{p}\rangle \ . \tag{42}$$

The existence of spatial periods of the problem has an important consequence on the structure of the master equation. Any dyad $|\vec{p}_1\rangle\langle\vec{p}_2|$, with $\vec{p}_i = \vec{q} + \vec{K}_i$ ($\hbar = 1$), is invariant under unitary transformation by $T(\vec{a})$ and can thus be coupled by time evolution only to dyads of the same form $|\vec{p}_1{}'\rangle\langle\vec{p}_2{}'|$, with $\vec{p}_i{}' = \vec{q}' + \vec{K}_i{}'$. In our integration of the master equation, we have to deal therefore only with the matrix elements of ρ between momentum vectors of the same Bloch vector, i.e., we are only concerned with the restriction of ρ inside each subspace of a given translational symmetry. These restrictions correspond to the following submatrices:

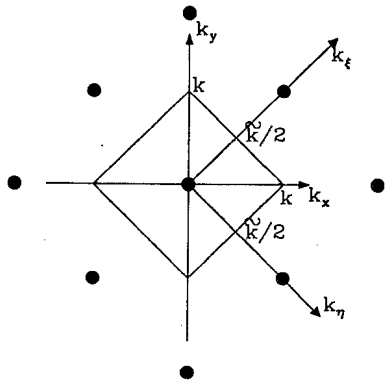

FIG. 6. The basic unit cell in reciprocal space, or the first Brilloun zone. Lattice vectors are indicated by the eight equivalent points, shown as filled circles.

$$\rho_{\vec{q}} \equiv \mathcal{P}_{\vec{q}}\rho\mathcal{P}_{\vec{q}} \quad \text{with} \quad \mathcal{P}_{\vec{q}} = \sum_{\vec{K}} |\vec{q}+\vec{K}\rangle\langle\vec{q}+\vec{K}| \ , \tag{43}$$

where the vector $\vec{K}$ belongs to the reciprocal lattice. The matrix elements of ρ between momenta of different Bloch vectors $\vec{q} \neq \vec{q}'$ are not coupled to the $\rho_{\vec{q}}$ and are expected to decay exponentially to 0 with time.

A priori a given $\rho_{\vec{q}}$ couples to all the $\rho_{\vec{q}'}$ matrices because of spontaneous emission, the Bloch vector shifting from $\vec{q}$ to

$$\vec{q}' = \vec{q} + \vec{k}_L - \vec{k}_S^{x,y} + \vec{K} \tag{44}$$

under the absorption of a laser photon of momentum $\hbar\vec{k}_L$ followed by the spontaneous emission of a photon of momentum $\hbar\vec{k}_S$. In Eq. (44), $\vec{k}_S^{x,y}$ is the projection of $\vec{k}_S$ on the xy plane and $\vec{K}$ is the appropriate vector of the reciprocal lattice bringing $\vec{q}+\vec{k}_L-\vec{k}_S^{x,y}$ back into the first Brillouin zone. For the simplified spontaneous emission pattern of Sec. II, we find that a given $\rho_{\vec{q}}$ is coupled to itself and to a single other $\rho_{\vec{q}'}$. Indeed, when $\vec{k}_S$ is along one of the laser axes x or y, $\vec{k}_L - \vec{k}_S$ is a vector of the reciprocal lattice and $\vec{q}' = \vec{q}$. If $\vec{k}_S$ is along the z axis, $\vec{k}_S^{x,y}$ vanishes and $\vec{q}' = \vec{q} - k\vec{e}_x$, up to a vector of the reciprocal lattice.

B. Reduction of the number of variables due to symmetries

The previously investigated spatial translations are not the only symmetries of our laser-field configuration. On the $J_g = 1/2 \to J_e = 3/2$ atomic transition considered here, one can combine the exchange of the ground-state sublevels $|\pm\rangle_z \to |\mp\rangle_z$ with the spatial translation of $\lambda/2$ along y, which exchanges the $\sigma_\pm$ components $\mathcal{E}_\pm$ of the laser electric field. In this way, the B_m operators in (9)

and the whole Liouvillian operator are clearly invariant under the action of

$$S_{\text{exch}} = (|+\rangle\langle -| + |-\rangle\langle +|)T(\lambda/2\vec{e}_y) \ . \tag{45}$$

We examine also the reflections inside the xy plane. As it is apparent in expression (1), the laser electric field is invariant by the reflections I_x and I_y with respect to the laser axes. From Eq. (9) we see that I_x and I_y are symmetry operators for the whole Liouvillian operator: the various operators B_m and our simplified spontaneous-emission pattern are unchanged under the action of I_x and I_y. For a general Bloch vector $\vec{q}$, this amounts to connecting the steady-state values of the matrices $\rho_{\vec{q}}$, $\rho_{I_x\vec{q}}$, $\rho_{I_y\vec{q}}$ and $\rho_{I_xI_y\vec{q}}$. One has, for example,

$$\rho^{(\text{st})}_{I_x\vec{q}} = I_x \rho^{(\text{st})}_{\vec{q}} I_x^\dagger \ . \tag{46}$$

Relations of the form (46) are particularly interesting when $\vec{q}$, $I_x\vec{q}$, $I_y\vec{q}$, and $I_xI_y\vec{q}$ coincide. This is found to be the case for one particular family of Bloch vectors only:

$$\vec{q} = \vec{0}, \quad \vec{q}' = -k\vec{e}_x \ . \tag{47}$$

In this section, we will restrict ourselves to this family.

For the particular value $\alpha = \pi/2$, to which all the explicit calculations of the present paper are restricted, $\mathcal{E}_+$ is invariant and $\mathcal{E}_-$ is changed into $-\mathcal{E}_-$ by a reflection in the ξ axis, so that the corresponding operator I_ξ is a symmetry operator. In this case, it is equivalent to introduce, instead of the set I_x, I_y, I_ξ, the symmetries $I_\xi, I_\eta = I_xI_yI_\xi$ and I_x.

We now want to deal numerically with the two coupled submatrices $\rho_{\vec{q}}$ defined in Eq. (43) with Bloch vectors $\vec{q} = 0$ and $\vec{q} = -k\vec{e}_x$. They are represented more conveniently in the following way:

$$\rho^{(\pm)}(n_\xi^{(1)}, n_\eta^{(1)}, n_\xi^{(2)}, n_\eta^{(2)}, i_q) \equiv \langle \pm, \vec{p}^{\,(1)}|\rho|\pm, \vec{p}^{\,(2)}\rangle \ , \tag{48}$$

with $\vec{p}^{\,(j)} = \hbar\tilde{k}(n_\xi^{(j)}\vec{e}_\xi + n_\eta^{(j)}\vec{e}_\eta) - \hbar k i_q \vec{e}_x$ $(j = 1, 2)$ and where $i_q = 0$ corresponds to $\vec{q} = 0$ and $i_q = 1$ to $\vec{q} = -k\vec{e}_x$. The truncation in momentum space is performed by restricting the indices in (48) to

$$-(n_{\max}+1) \le n_\xi^{(1)}, n_\eta^{(1)}, n_\xi^{(2)}, n_\eta^{(2)} \le n_{\max}+1 \ . \tag{49}$$

We take absorbing boundary conditions, assuming that the density matrix is vanishing on the boundary of the domain (49), i.e., when one of the indices $n_{\xi,\eta}^{(1,2)}$ equals $\pm(n_{\max}+1)$.

We restrict ourselves to initial density matrices $\rho_{\vec{q}}(0)$ ($\vec{q} = \vec{0}$ or $-k\vec{e}_x$) invariant by all the symmetry operators S we have considered:

$$S\rho_{\vec{q}}(0)S^\dagger = \rho_{\vec{q}}(0) \ . \tag{50}$$

Equation (36) then ensures that $\rho_{\vec{q}}(t)$ is invariant by S for any later time t. This observation leads to the following reduction of the problem.

First, through the S_{exch} transformation given in (45), one can express the density matrix in the $|-\rangle_z$ ground-state sublevel as function of the density matrix in the $|+\rangle_z$ sublevel. Considering the matrix elements of both sides of (50) between $|-,\vec{p}_1\rangle$ and $|-,\vec{p}_2\rangle$, with $S = S_{\text{exch}}$, and using (37), one gets indeed:

$$\rho^{(-)}(n_\xi^{(1)}, n_\eta^{(1)}, n_\xi^{(2)}, n_\eta^{(2)}, i_q)$$

$$= (-1)^{i_{\text{exch}}}\rho^{(+)}(n_\xi^{(1)}, n_\eta^{(1)}, n_\xi^{(2)}, n_\eta^{(2)}, i_q) \ , \tag{51}$$

with $i_{\text{exch}} = n_\xi^{(1)} + n_\eta^{(1)} + n_\xi^{(2)} + n_\eta^{(2)}$. This reduces the number of components of ρ by a factor of 2 and we omit the superscript $\pm$.

Then, setting S equal to each of the symmetry operators $I_\xi, I_\eta, I_\xi I_\eta$, and I_x, we find that it is sufficient to consider elements of ρ with $n_\eta^{(1)} \ge n_\xi^{(1)} \ge 0$. This leads to an additional reduction of the number of components by a factor of 8.

C. Numerical implementation

In our program, we consider as independent components of ρ the matrix elements with an internal state $|+\rangle_z$ and with indices $n_\eta^{(1)} \ge n_\xi^{(1)} \ge 0$ in the domain (49). The number of such components, with $i_q = 0, 1$, is

$$N = (2n_{\max}+3)^2(n_{\max}+2)(n_{\max}+3), \tag{52}$$

a factor almost 16 smaller than the original number $4(2n_{\max}+3)^4$. For the largest $n_{\max}$ we have considered ($n_{\max} = 15$), N is on the order of 3×10^5. In order to take into account in an automatic way the previous symmetry relations, ρ is represented numerically as a one-dimensional complex array with N components:

$$A(k) \equiv \rho(n_\xi^{(1)}, n_\eta^{(1)}, n_\xi^{(2)}, n_\eta^{(2)}, i_q) \quad \text{for } 1 \le k \le N \ , \tag{53}$$

where k is an integer function of the $n_{\xi,\eta}^{(1,2)}$ and i_q indices

$$k = f(n_\xi^{(1)}, n_\eta^{(1)}, n_\xi^{(2)}, n_\eta^{(2)}, i_q). \tag{54}$$

This function f is defined on the whole set (49) and includes all the symmetries.

Numerically, the quantum master equation reduces to a first-order ordinary differential equation, with time-independent coefficients, on the N components vector A:

$$\frac{d}{dt}A = M[A] \ . \tag{55}$$

If one keeps only the nonzero coefficients of M, the evaluation of any component $M[A](k)$ requires a small number of multiplications, on the order of 100. In addition, all the nondiagonal multiplicative factors $M(k,k')$ originate only from the atom-laser interaction. Therefore, they do not depend on the atomic momentum indices, i.e., on k, up to a permutation, and they can be stored without requiring a lot of memory. For instance, the contribution of the optical potential U_+ to the evolution of $\rho^{(+)}$, i.e.,

$(1/i\hbar)[U_+, \rho^{(+)}]$, involves a coupling of a given $A(k)$ to itself and to 16 neighboring states in momentum space.

The solution of the differential equation (55) is approximated numerically by a fourth-order Taylor expansion of the exact propagator between t and $t+dt$:

$$e^{Mdt} \simeq 1 + Mdt + (Mdt)^2/2 + (Mdt)^3/6 + (Mdt)^4/24 . \quad (56)$$

Expression (56) requires four evaluations of the action of M on A. The condition of stability of this scheme is

$$|1 + \mu dt + (\mu dt)^2/2 + (\mu dt)^3/6 + (\mu dt)^4/24| < 1 \quad (57)$$

for any eigenvalue μ of the matrix M. Physically, we expect the maximal real part $\gamma_{\max}$ of the μ's to be on the order of the typical excitation rate Γs_0 of the atoms by the laser field and the maximal imaginary part $\omega_{\max}$ of the μ's on the order of the largest Bohr frequencies of the Hamiltonian (4). An overestimate of $\omega_{\max}$ is obtained as the sum of the maximum Bohr frequencies of $\vec{p}^2/2M$ on the finite sample (49) and V:

$$\omega_{\max} \leq \bar{\omega}_{\max} = \frac{\hbar \tilde{k}^2}{2M}(2n_{\max}^2) + 4|\delta| s_0 . \quad (58)$$

We are mainly in a regime of large detunings ($|\delta| \gg \Gamma$), so that $\omega_{\max}$ is much larger than $\gamma_{\max}$. One therefore solves (57) for $\mu = i\omega$, ω real, which gives

$$|\omega dt| < 2\sqrt{2} . \quad (59)$$

We finally keep as an approximation for the maximum acceptable time step

$$dt_{\max} = \frac{2\sqrt{2}}{\bar{\omega}_{\max}} . \quad (60)$$

In our numerical calculations, we have made the choice of time step $dt = dt_{\max}$, assuring the convergence of the time evolution. In this way, the time evolution of the matrix elements of ρ between eigenstates $|1\rangle$ and $|2\rangle$ of H with an energy difference $E_2 - E_1 \sim \hbar\omega_{\max}$ is not accurate, but the fast oscillation terms $\langle 1|\rho|2\rangle$ are rapidly damped to a value smaller than a population $\langle 1|\rho|1\rangle$ or $\langle 2|\rho|2\rangle$ by a factor $\hbar\gamma_{\max}/|E_2 - E_1| \sim \gamma_{\max}/\omega_{\max} \ll 1$.

We have also introduced an algorithm for the time evolution relying on a splitting formula

$$e^{Mdt} \simeq e^{\mathcal{H}dt/2}(1 + \mathcal{R}dt)e^{\mathcal{H}dt/2} , \quad (61)$$

where $\mathcal{H}$ stands for the Hamiltonian part of the Liouvillian and $\mathcal{R}$ represents $\mathcal{L}_{\text{relax}}$. The $\exp(\mathcal{H}dt/2)$ terms are expanded to order 4 in dt. Note that $\mathcal{R}$ is not treated to the same order in (61). This is legitimate since the rates in $\mathcal{R}$ are much smaller than the Bohr frequencies in $\mathcal{H}$. In this way, the relaxation part, which requires more multiplications than the Hamiltonian part, is evaluated only once per time step dt and the total calculation time is reduced. The numerical results derived from this splitting technique with the time step $dt = 2dt_{\max}$ are found to be in good agreement with the ones of the full fourth-order scheme with the smaller time step $dt_{\max}$.

The results derived from the numerical integration of the master equation will be presented in Sec. VI and compared to the prediction of the other approaches used in this paper.

V. SECULAR METHOD

We now come to the secular approach, which is the last method that we have used to study the 2D Sisyphus cooling. It consists in determining perturbatively the steady state of the cooled atoms in three steps. First we find the eigenstates ϕ_i and the eigenenergies E_i of the Hamiltonian H entering in the master equation (3). We then include the relaxation part of the master equation by calculating the rates of transfer γ_{ij} between any two eigenstates ϕ_i and ϕ_j. Finally the steady state is characterized by the set of populations π_i of the eigenstates which balance the rate equations

$$0 = \dot{\pi}_i = -\sum_j \gamma_{i\to j}\pi_i + \sum_j \gamma_{j\to i}\pi_j . \quad (62)$$

All the relevant steady-state quantities, such as position or momentum distributions, can then be deduced from this set of populations and the known eigenstates.

This solution is only an approximation of the real steady-state density matrix since it amounts to neglecting any nondiagonal matrix element $\langle\phi_i|\rho|\phi_j\rangle$ between two different eigenstates of H. In steady state, we have (3)

$$0 = \frac{i(E_j - E_i)}{\hbar}\langle\phi_i|\rho|\phi_j\rangle + \langle\phi_i|(\dot{\rho})_{\text{relax}}|\phi_j\rangle . \quad (63)$$

Consequently the secular approximation is valid if, for any pair ϕ_i, ϕ_j with $i \neq j$, the steady-state value of $\langle\phi_i|\rho|\phi_j\rangle$ can be assigned to 0 by symmetry reasons or if the Bohr frequency $(E_j - E_i)/\hbar$ is much larger than the transition rates ($\sim \Gamma s_0$) originating from $(\dot{\rho})_{\text{relax}}$. Below we shall demonstrate that the relevant minimal Bohr frequencies of H are of the order of the recoil shift $E_R/\hbar$. The secular approximation is then valid if

$$\hbar\Gamma s_0 \ll E_R \Longleftrightarrow u_0 \ll |\delta|/\Gamma . \quad (64)$$

This condition implies very large detunings for a given light-shift potential. It is much more restrictive than the one required in 1D [6]:

$$\hbar\Gamma s_0 \ll \sqrt{u_0}E_R \Longleftrightarrow \sqrt{u_0} \ll \delta/\Gamma . \quad (65)$$

The reason for this change is simply the increase of degeneracy when one passes from 1D to 2D. For instance, for a given Bloch vector and in the energy range between $-u_0E_R$ and 0, corresponding to the bound levels, there are $u_0E_R/\hbar\Omega_{\text{osc}} \sim \sqrt{u_0}$ states in 1D and $(u_0E_R/\hbar\Omega_{\text{osc}})^2/2 \sim u_0$ states in 2D. The average splitting between these levels therefore is reduced from $\sim \sqrt{u_0}E_R$ in 1D to $\sim E_R$ in 2D. A similar argument on the density of states in the three-dimensional case shows that the Bohr frequencies between adjacent states could be

very small, much smaller than the recoil energy. Consequently, the secular approach will probably be very hard to use in 3D.

A. Eigenstates and the energy spectrum

Here the diagonalization of the Hamiltonian H given in (4) is considered. Since V is diagonal in the basis (g_+, g_-), each eigenstate factorizes into an internal atomic part $|g_\pm\rangle$ times an external part, which is an eigenstate of $H_\pm$:

$$H_\pm = \frac{p^2}{2M} + 4\hbar\delta s_0 V_\pm(k\vec{r}) \ . \tag{66}$$

We note that the relation $V_-(kx, ky) = V_+(kx, ky + \pi)$ implies that the spectra of H_+ and H_- are identical and that the eigenstates of H_- can be deduced from those of H_+ by a spatial translation.

In order to exploit the symmetries of $V_\pm$, we use the coordinates (ξ, η) corresponding to the rotated basis (32) and (33). In Fig. 7(a) we show a surface plot of V_+. The potential has two types of minima, global ones of value -1 situated at $(\xi, \eta) = (n\tilde{\lambda}, m\tilde{\lambda})$ and local ones of value $-1/3$ in positions $(\xi, \eta) = ((n+1/2)\tilde{\lambda}, (m+1/2)\tilde{\lambda})$. The maxima, where $V_+(\xi, \eta) = 0$, are attained at points such as $(\xi, \eta) = (n\tilde{\lambda}, (m+1/2)\tilde{\lambda})$ or $(\xi, \eta) = ((n+1/2)\tilde{\lambda}, m\tilde{\lambda})$. As deduced from the translational symmetry between V_+ and V_-, the global minima of V_+ coincide with the local minima of V_-, whereas the maxima for the two potentials are at the same locations.

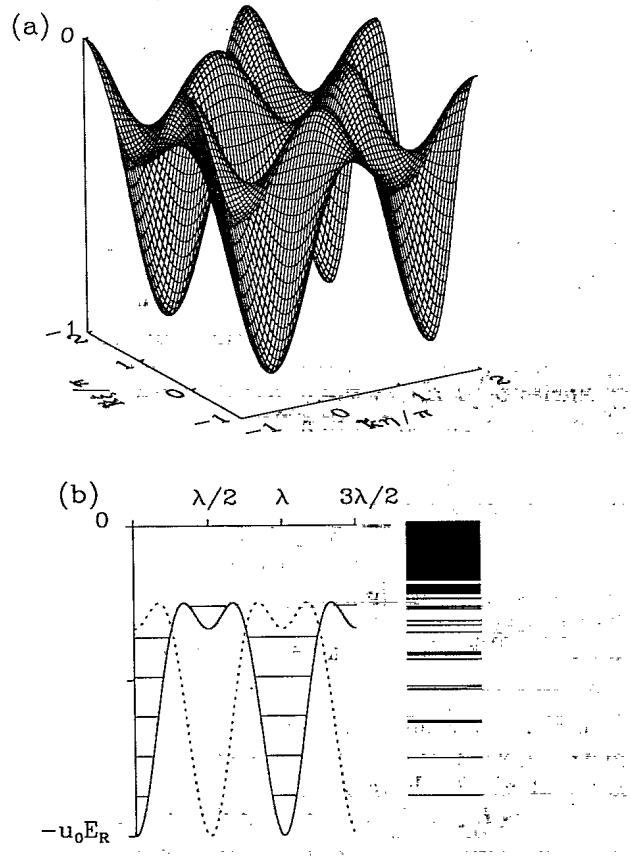

FIG. 7. (a) A surface plot of the potential V_+ and (b) the energy spectrum for $u_0 = 123$ shown together with a cut through the potential V_+ along the line $\xi = \eta$, with 2D harmonic levels indicated. The dotted line shows the analog variation of V_-.

As it is known from the Bloch theorem, each eigenstate of $H_\pm$ can be written as a product of a periodic function of ξ and η with period $\tilde{\lambda}$, times a plane wave $\exp(i\vec{q}\cdot\vec{r})$, where the Bloch vector $\vec{q}$ is chosen in the first Brillouin zone (40). The energy spectrum consists of allowed energy bands separated by forbidden gaps. An example is plotted in Fig. 7(b) for $u_0 = 123$. For comparison, the variations of V_+ along the line $\xi = \eta$ (i.e., $y = 0$) with harmonic levels are indicated. There is clearly a one-to-one correspondence between the lowest energy bands and the lowest harmonic levels in the main potential well. The harmonic oscillation frequency in the main potential well equals

$$\Omega_{\rm osc} = \sqrt{2u_0}\frac{E_R}{\hbar} \tag{67}$$

[see Eq. (29)] and the one corresponding to the harmonic approximation of the local minimum is

$$\Omega'_{\rm osc} = \sqrt{\frac{2u_0}{3}}\frac{E_R}{\hbar} \ . \tag{68}$$

In Fig. 7(b), an energy band corresponding to the first bound level in the local potential well can also be identified. To emphasize this point, we have shown in Fig. 8, as a function of u_0, the eigenenergies of H for the given Bloch vector $\vec{q} = (k/4)\vec{e}_x$. One notes the existence in the low part of the spectrum of energies with different slopes, the first ones corresponding to states localized around the bottom of the global potential minimum and varying as

$$\frac{E_N}{E_R} \simeq (N+1)\frac{\hbar\Omega_{\rm osc}}{E_R} - u_0 = (N+1)\sqrt{2u_0} - u_0, \qquad N \geq 0 \tag{69}$$

and the second ones to states localized around the bottom of the local potential minimum and varying as

$$\frac{E'_N}{E_R} \simeq (N'+1)\frac{\hbar\Omega'_{\rm osc}}{E_R} - \frac{u_0}{3} = (N'+1)\sqrt{\frac{2u_0}{3}} - \frac{u_0}{3} \ . \tag{70}$$

Avoided crossings between states of these two types can appear for certain values of the potential depth, i.e., $u_0 \simeq 85$ or $u_0 \simeq 120$, when the eigenenergies of two states, one of each class, come close. Figure 9 shows density plots in one spatial period of the wave functions participating in the avoided crossing around $u_0 = 120$, shown for three values of the potential depth "before," "at," and "after" the avoided crossing. Before and after the avoided crossing, one clearly identifies the two types of states, each being localized around a potential minimum. At the avoided crossing, tunneling through the barrier separating the two wells causes a mixing of the two types of states so that the two eigenstates of $H_\pm$ are

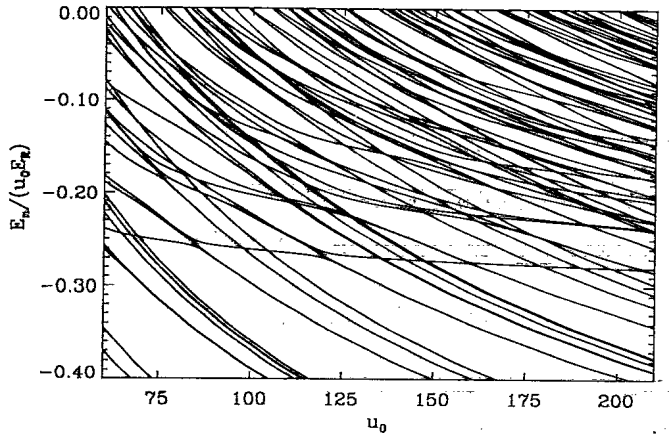

FIG. 8. The eigenenergies calculated for a Bloch vector $\vec{q} = (k/4)\vec{e}_x$ in a range just below zero, shown as a function of u_0. The eigenenergies are given in units of u_0E_R. One observes several avoided crossings. In particular, around $u_0 \sim 85$ or $u_0 \sim 120$ an avoided crossing involving the first bound state in the local potential minimum appears.

delocalized between the two wells. A third state also appears in Fig. 8, with an energy between the two levels participating in the avoided crossing. This third state does not couple to the two other levels because of its different symmetry.

B. Degenerate and quasidegenerate levels

Since the validity of the secular approximation requires Bohr frequencies $(E_j - E_i)/\hbar$ large compared to the relaxation rates, the quasidegeneracies that may occur in the spectrum of H deserve particular attention.

The first example of quasidegeneracy occurs for two states belonging to the same band, with different Bloch vectors. Fortunately, the translational invariance of the problem along the square lattice of step $\tilde{\lambda}$ implies that the steady-state density matrix is also invariant under these translations. Therefore no steady-state matrix element can exist between two states corresponding to different Bloch vectors and we do not have to worry about such closely spaced energy levels.

We now choose a given Bloch vector and we review the quasidegeneracies that may appear in the spectrum of $H_\pm$ for this $\vec{q}$. In the low part of the spectrum, the width of the energy bands is so small that the quasidegeneracies can be investigated for the particular value $\vec{q} = \vec{0}$ only. Then the eigenvalue problem has a noncommutative group of symmetries, the so-called C_{4v} group, generated by the reflections I_x and I_y with respect to the laser axes (see Sec. IV) and the reflection I_ξ with respect to the ξ axis. According to Wigner's theorem, the systematic degeneracies are given by the dimension of the irreducible representations of the symmetry group

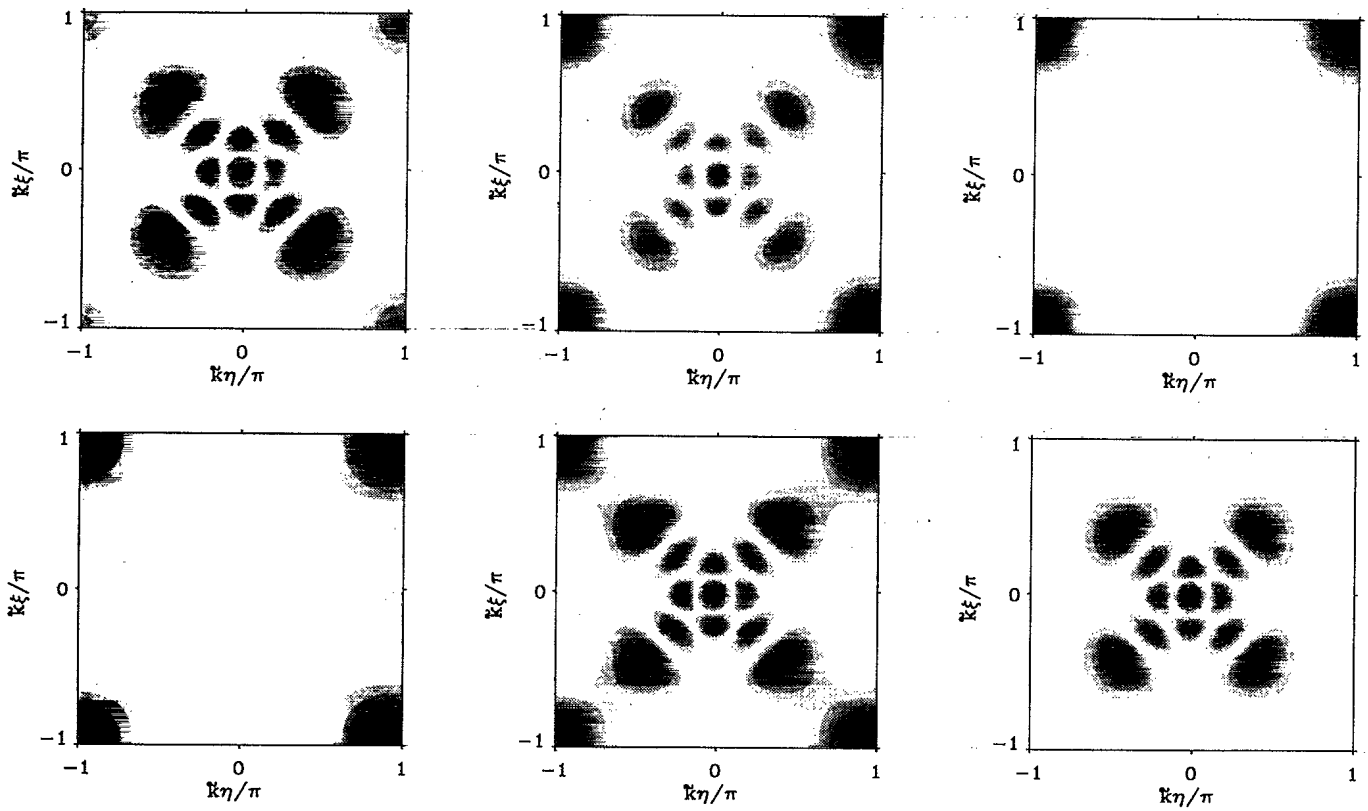

FIG. 9. Density plots of the wave functions participating in the avoided crossing around $u_0 \sim 120$, with band indices $n = 21$ and $n = 23$ ($n = 0$ corresponds to the ground state). The wave functions in the upper row correspond to $n = 23$ for values of u_0 equal to 111, 120, and 123 from left to right. The coexistence of two spatial components in each eigenstate for $u_0 = 120$ is quite clear.

in the Hilbert space. Two kinds of irreducible representations are found. The first one involves one-dimensional invariant subspaces, corresponding to eigenvectors of H with the same symmetry with respect to I_x and I_y. It leads to no systematic degeneracy. The second kind involves invariant subspaces of dimension 2, giving rise to a twofold degenerate eigenvalue of H. The corresponding eigenvectors $|1\rangle$ and $|2\rangle$ can be chosen with opposite symmetries with respect to I_x and I_y. These two eigenvectors are interchanged by the action of I_ξ (i.e., $|2\rangle = I_\xi|1\rangle$). As the steady-state density matrix ρ^{st} is invariant under the symmetries I_x and I_y, the matrix element $\langle 1|\rho^{st}|2\rangle$ vanishes. The invariance with respect to I_ξ, on the other hand, ensures that the populations $\langle 1|\rho^{st}|1\rangle$ and $\langle 2|\rho^{st}|2\rangle$ are equal.

In order to estimate the minimum energy gap between the lowest lying bands, we perform an expansion of the problem in powers of the Lamb-Dicke parameter ka_0, where a_0 is the spatial extension of the ground state

$$ka_0 = \frac{1}{(2u_0)^{1/4}} . \tag{71}$$

To second order, the 2D harmonic oscillator spectrum is recovered. $(N+1)$-fold degenerate levels are bunched in multiplicities $\mathcal{E}_N$ located at energies $(N+1)\hbar\Omega_{\rm osc}$ above the bottom of the well ($N \geq 0$). To fourth order in ka_0, this degeneracy is partially lifted, as expected from the previous symmetry considerations. The resulting energy splitting is proportional to $u_0 E_R (ka_0)^4$, i.e., it is equal to the recoil energy E_R up to a numerical factor. For instance, the multiplicity located around $4\hbar\Omega_{\rm osc}$, which would be 4 times degenerate for a pure harmonic potential, is split into two submultiplicities separated by $(\sqrt{13}/3)\ E_R$, with each containing two levels.

Still considering a given Bloch vector $\vec{q}$, a second type of quasidegeneracy appears in the region where the two types of bound states mentioned above may participate in an avoided crossing. Here again the average splitting between the two levels participating in the avoided crossing is found numerically to be on the order of the recoil energy.

Finally, the last kind of quasidegeneracy that appears in the spectrum of H for a given $\vec{q}$ concerns the states corresponding to quasifree motion, with an energy larger than the modulation of the light-shift potential. Since the Bloch vector is fixed, we have one state in each square of area $(\hbar\tilde{k})^2 = 2\hbar^2k^2$. Thus, in this 2D case, the density of states dn/dE equals $\pi/2E_R$, which indicates that the average distance between two consecutive states[2] is again on the order of the recoil energy E_R.

[2]In fact, we observe that the states in the continuum appear in groups of 4, corresponding to channeling of the atoms along the symmetry axes $\pm x, \pm y$ or $\pm\eta, \pm\xi$, and we have degenerate levels but of different symmetry properties. Going very high in energy, we also find states in groups of 8, corresponding to motion along four axes "far from" the symmetry axes, i.e., motion along $(x,y) = (\pm n, \pm m), (\pm n, \mp m), (\pm m, \pm n), (\pm m, \mp n)$ with a ratio between m and n being far from 0 and 1 ($m < n$).

C. Rate equations

We now turn to the problem of calculating the rates of transfer $\gamma_{i\to j}$ between any two eigenstates ϕ_i and ϕ_j. In the secular regime, these rates will lead to the steady-state populations of the ϕ_i's.

The rate $\gamma_{i\to j}$ is obtained directly by calculating $\dot{\pi}_j$, assuming that the atom is initially in state ϕ_i. Using (3) and (8), we get

$$\gamma_{i\to j} = \Gamma s_0 \langle\phi_j|\ \mathcal{L}_{\rm relax}\left(|\phi_i\rangle\langle\phi_i|,\ k\vec{r}\right)\ |\phi_j\rangle\ . \tag{72}$$

We now replace the relaxation operator $\mathcal{L}_{\rm relax}$ by its expression (9) to derive, for $i \neq j$,

$$\gamma_{i\to j}(\pm\to\pm) = \frac{\Gamma s_0}{8} \sum_{m=x,y} \sum_{\epsilon} \sum_{l\neq m} |\langle\phi_j|e^{-ik\epsilon r_l} B_m|\phi_i\rangle|^2\ , \tag{73}$$

if ϕ_i and ϕ_j correspond to the same internal state of the atom, and

$$\gamma_{i\to j}(\pm\to\mp) = \frac{\Gamma s_0}{8} \sum_{\epsilon} \sum_{l=x,y} |\langle\phi_j|e^{-ik\epsilon r_l} B_z|\phi_i\rangle|^2\ , \tag{74}$$

if ϕ_i and ϕ_j correspond to different internal states.

In order to discuss the dynamics of the cooling process, we may, as a simple approximation, consider the transition rates for three processes only: heating of the lowest levels of a given potential, say U_+, towards either (i) eigenstates of U_- or (ii) neighboring states in U_+ and (iii) cooling by transitions of hot atoms in, e.g., U_+ towards bound states of U_-.

The heating processes are considered in the case of deep potential wells, for the atoms occupying the lowest lying levels. These atoms are in the Lamb-Dicke regime and a good approximation of the corresponding eigenfunctions are the 2D harmonic oscillator wave functions. The heating of an atom in a localized eigenstate of H_+, say, takes place by two processes: one is the transition towards the other bound states of g_+ of higher energy and the other is the departure towards eigenstates of H_-, also with higher energy. Here we wish to discuss the dependence of these rates on the potential depth parameter u_0.

Consider first the total departure rate from a bound state of U_+ towards all eigenstates of H_-. The rate for such a process is found from the expression in (74). When we sum the transition rate over the full set of states $|j,-\rangle$, we find that the total departure is given by a matrix element

$$\left(\frac{d\pi_{i,+}}{dt}\right)_{\rm dep\to -} = \frac{\Gamma s_0}{9} \langle\phi_i\,||\mathcal{E}_-|^2|\,\phi_i\rangle \pi_{i,+}\ . \tag{75}$$

In the Lamb-Dicke regime, $\mathcal{E}_-$ is approximated by quadratic terms in x and y and the term (75) is proportional to $(ka_0)^4\Gamma s_0 = \Gamma s_0/(2u_0)$. The corresponding time scale for heating to take place by this process is rather slow. Compared to the results of [18] for one-

dimensional Sisyphus cooling (rate $\sim \Gamma s_0/\sqrt{u_0}$), we find that in our 2D system, the rate of this specific heating process is reduced by a factor of $\sqrt{u_0}$.

For the transitions between states of the same internal state, i.e., g_+, we see from Eq. (73) that in the Lamb-Dicke regime, the rates involve squared matrix elements of operators such as $p_S x/\hbar$, where $p_S = \epsilon\hbar k$ is the momentum of the fluorescence photon. If we approximate in (73) the ϕ's by harmonic oscillator eigenstates $|n_x, n_y\rangle$, we deduce that the rates from and to a state $|n_x, n_y\rangle$ toward and from the state $|n_x+1, n_y\rangle$ are $\gamma_0(n_x+1)$, where

$$\gamma_0 = 2(ka_0)^2\Gamma s_0 = \frac{\sqrt{2}\Gamma s_0}{\sqrt{u_0}} . \tag{76}$$

These rates have therefore the same dependence on u_0 as in 1D.

The heating brings the atom to the quasifree states of H_+, which are spread out more or less uniformly in space. Now the atom has a rate of transition to the internal sublevel $|-\rangle$ on the order of the optical pumping rate Γs_0. These transitions can lead to Sisyphus cooling.

For the heating part of the Sisyphus dynamics, we would like to give an estimate of the mean time for the heating to bring the atom from the ground state of the optical potential to states of positive energy. As discussed above, a first heating process implies a direct transition to a state of opposite internal level and the corresponding time scales as $u_0/(\Gamma s_0)$. The second process involves energy increments of $\hbar\Omega_{\rm osc}$ by transitions between neighboring states within the same potential well. In order to estimate the time scale for this process, let us consider the mean change in harmonic oscillator index $n = n_x + n_y$ after a small time step dt. Starting from the state $|n_x, n_y\rangle$ at time t, we have at time $t + dt$ and to first order in dt a departure probability towards the multiplicity $\{|n_x+1, n_y\rangle, |n_x, n_y+1\rangle\}$ (increase of n by 1) given by $\gamma_0(n_x+1)dt + \gamma_0(n_y+1)dt = \gamma_0(n+2)dt$. Similarly the departure probability towards the multiplicity $\{|n_x-1, n_y\rangle, |n_x, n_y-1\rangle\}$ (decrease of n by 1) is $\gamma_0 n dt$. Therefore the mean change in $n = n_x + n_y$ corresponds to

$$\frac{d}{dt}\langle n\rangle = 2\gamma_0 . \tag{77}$$

We consider the atom to be at the top of the potential when n is on the order of $\sqrt{u_0}$ leading to a mean heating time $\sim \sqrt{u_0}/\gamma_0 \sim u_0/(\Gamma s_0)$.

This time scale can be recovered in a semiclassical picture. It corresponds to the time required for an atom performing a random walk in momentum space, with a momentum diffusion coefficient $D_{++} \sim (\hbar k)^2\Gamma s_0$ given in (23), to experience a mean increase in energy on the order of $u_0 E_R$.

Finally, we consider the time scale of the whole Sisyphus dynamics in the present regime $u_0 \gg 1$. The atomic motion in steady state involves random successions of two different processes: a slow heating from the lowest lying levels up to states of positive energy and a fast cooling from these high energy states back to the bottom of the potential wells. The relaxation time for average quantities such as the atomic kinetic energy is mainly determined by the slow heating process. It is therefore expected to scale as $u_0/\Gamma s_0$, which is in agreement with the semiclassical results presented in Sec. III C and which is longer than the corresponding 1D result $\sqrt{u_0}/(\Gamma s_0)$ [18,19].

D. The steady-state distribution

We have calculated numerically the steady state of the set of equations (62), associated with the normalization condition $\sum \Pi_i = 1$. Since all rates are proportional to Γs_0, this term factorizes out of (62) and we are left with a set of equations depending only on u_0. In the secular regime, there is therefore a single universal parameter to characterize the steady state instead of the two parameters generally required.

In order to reduce the computational effort, our calculations were performed for a specific choice of the Bloch vectors. With the simplified spontaneous-emission spectrum, only states of Bloch vectors $\vec{q}_1$ and $\vec{q}_2 = \vec{q}_1 - k\vec{e}_x$ couple. We have chosen to perform the calculations for two different pairs $(\vec{q}_1, \vec{q}_2)$ in a way that describes the whole first Brillouin zone best, i.e., we have made use of the symmetries in the problem mentioned in Sec. IV. We have therefore chosen $\vec{q}_1 = k/2\vec{e}_x + k/4\vec{e}_y, \vec{q}_2 = -k/2\vec{e}_x + k/4\vec{e}_y$ and $\vec{q}_1 = k/4\vec{e}_x, \vec{q}_2 = -3k/4\vec{e}_x$, which amounts to paving the Brillouin zone into 16 equal squares. We have calculated the periodic function appearing in the Bloch eigenstate with a cutoff in the Fourier series at a momentum $|p_\xi| = |p_\eta| = n_{\max}\hbar\tilde{k} = n_{\max}\sqrt{2}\hbar k$. In most of the calculations of this section, we have taken as a cutoff parameter $n_{\max} = 15$, which is exactly the one used in the truncated classical Monte Carlo calculations of Sec. III D [see Eq. (31)]. Note that all the calculated eigenstates are included in the numerical solution of the rate equations, so that the total number of energy bands considered per atomic internal state is $(2n_{\max}+1)^2 = 961$. This is an improvement by a factor of roughly 2 with respect to the results presented in [11], for which the cutoff parameter was $n_{\max} = 10$ and the corresponding number of energy bands was only $21^2 = 441$.

In Fig. 10 we show the populations of the first ten bands as a function of the potential depth u_0. A remarkable feature of the variations of π_0 as a function of u_0 is the appearance of resonances. Their physical origin is discussed in detail in Sec. V E. Here we argue that the resonant features in π_0 are not an artifact of the truncation in momentum space.

Consider the resonance in π_0 located around $u_0 = 120$. We know from the analytical solution of Appendix B that the steady-state density matrix is normalizable ($u_0 > 33$), so that the population π_0 of the lowest energy band has a nonvanishing limit for $n_{\max}$ going to infinity. We also know from Appendix B and from the numerical results of Sec. III that the mean square momentum is diverging when $n_{\max}$ is increased. These two quantities π_0 and $\langle p^2\rangle/(\hbar k)^2$ are given as functions of the cutoff parameter $n_{\max}$ in Table I, for three values of u_0 around 120. When $n_{\max}$ shifts from 15 to 21, which corresponds to a number of bands in the calculation shifting from 961 to

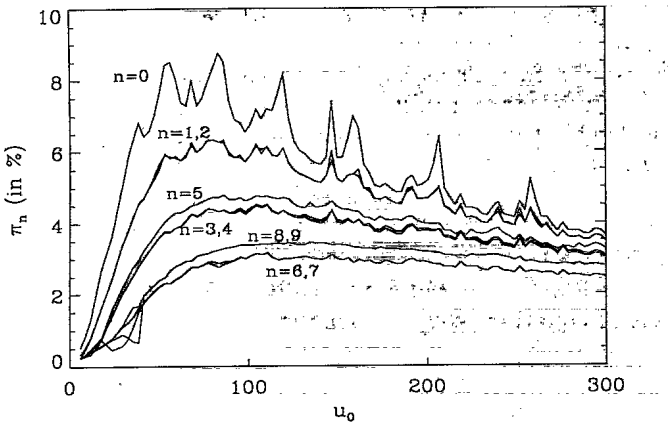

FIG. 10. The populations in the lower ten bands, shown as a function of u_0, with a truncation in momentum space as in Eq. (31). We note the resonances, especially in π_0.

TABLE I. The effect of the momentum cutoff parameter n_{max} on the population π_0 of the lowest energy band and on the mean square momentum in recoil units $\langle p^2\rangle/(\hbar k)^2$, in the secular approach. The values of u_0 that we consider are bracketing a resonance in π_0.

u_0	n_{max}	$10^2\pi_0$	$\langle p^2\rangle/(\hbar k)^2$
114	15	7.14	37.2
	18	7.11	40.4
	21	7.08	43.1
120	15	8.19	36.6
	18	8.16	38.6
	21	8.14	40.7
126	15	6.29	38.5
	18	6.27	40.5
	21	6.25	42.5

1849, the decrease in π_0 is on the order of 5×10^{-4} (relative change less than 2%). The same change in n_{max} leads to a much larger relative increase (greater than 11%) of $\langle p^2\rangle/(\hbar k)^2$. We are therefore confident that the truncation effect on π_0 remains small and that it is smaller than the observed variation of π_0 through a resonance.

From the steady-state populations, we can also extract momentum and position distributions. A position distribution has been given in [11]: it exhibits a strong modulation of the spatial atomic density.

Figure 11(a) shows a momentum distribution, obtained for $u_0 = 60$. We observe an anisotropy in the wings, corresponding to an accumulation of atoms along the rotated axes ξ and η. We recover here a feature that we have discussed in detail in the classical Monte Carlo analysis of the cooling process. This feature is reduced for larger values of u_0 as shown in Fig. 11(b) for $u_0 = 210$. Finally, in Fig. 12, we have indicated the variation with u_0 of the half widths $p_{e,x}$ and $p_{e,\xi}$ defined in Sec. III C.

E. A simple model of the resonances in π_0

As we have already noted [11], a remarkable feature appears in the variations of the populations of the states ϕ_i with u_0, namely, the resonances in especially π_0. This resonant behavior of π_0 is due to the existence of the avoided crossings, induced by tunneling, in the energy diagram (cf. Fig. 8). To get some physical insight into this problem, we consider the following simple model including four levels $0, a, b$, and 1 (see Fig. 13). Level $|0\rangle$ is the ground state in, e.g., U_-; $|a\rangle$ and $|b\rangle$ are the two spatial components of the states that participate in the avoided crossing: $|a\rangle$ is localized around the local minimum of U_+ and $|b\rangle$ is localized in the main potential well of U_+; finally, $|1\rangle$ symbolizes the rest of the states in the problem.

At a position where the eigenenergies differ significantly, no effects of the avoided crossing appear and the transitions between the four levels take place between the "pure" states $0, a, b$, and 1. Level $|a\rangle$ is a state in the local potential minimum of U_+ and it has a large transition rate toward the ground state $|0\rangle$, but the rate of feeding $\gamma_{1\to a}$ is low. This is due to the fact that state $|a\rangle$ differs in spatial dependence from the rest of the excited levels. Level $|b\rangle$ has a feeding rate $\gamma_{1\to b}$ of "typical" size, i.e., larger than $\gamma_{1\to a}$, and departs mainly toward levels other than $|0\rangle$, i.e., its departure is determined by $\gamma_{b\to1}$, which is large. The ground state departs toward the ensemble of the other states $|1\rangle$.

When the energy levels participating in the avoided crossing come closer, the two spatial components $|a\rangle$ and $|b\rangle$ start to mix in the eigenstates because of tunneling between the two adjacent wells. This mixing was well

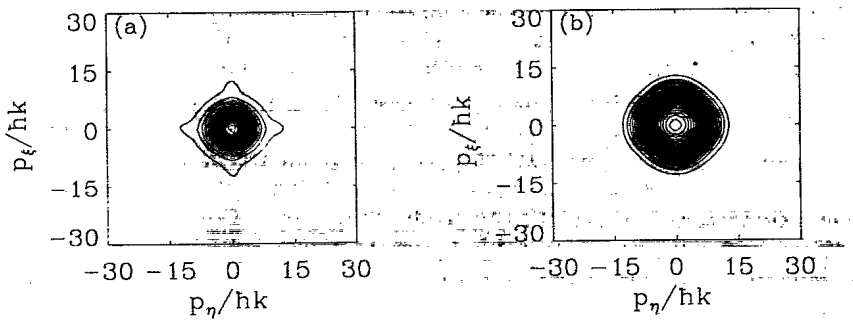

FIG. 11. The momentum distribution calculated for (a) $u_0 = 60$ and (b) $u_0 = 210$ with a truncation in momentum space such that n_{max} in Eq. (31) equals 18. The channeling lines found in Fig. 4 are also apparent here, for the low value of u_0 in (a).

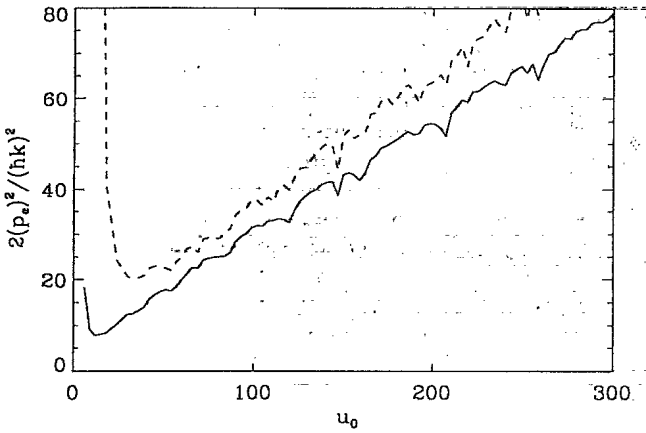

FIG. 12. The variation of the half widths squared $p^2_{e,x}$ (in dashed line) and $p^2_{e,\xi}$ (in solid line) as a function of u_0 calculated within the secular approach. The same truncation is applied as in Eq. (31).

illustrated by the density plot of the wave functions of Fig. 9. At the center of the avoided crossing, the transitions take place between the completely mixed states $(1/\sqrt{2})(|a\rangle \pm |b\rangle)$ and the states $|0\rangle$ and $|1\rangle$. The rate of feeding of each of the two mixed states is now on the order of half the rate of feeding of the state $|b\rangle$ whereas the departure toward the lower state $|0\rangle$ is on the order of half the original departure of state $|a\rangle$. Therefore the mixed states have both a large feeding from the upper states and a large transfer toward the ground state. As a consequence, the population in the ground state increases noticeably while the sum of the population of the states participating in the avoided crossing remains small and practically unchanged. The pair of states $|a\rangle$ and $|b\rangle$ merely acts as a "tap," opening an extra channel in the feeding of the state $|0\rangle$.

VI. COMPARISON

In this paper, we have presented three different methods for the analysis of 2D laser cooling. Two of these methods involve approximations of the exact quantum master equation. One is the classical limit for the atomic motion that was presented in Sec. III and the other is the reduction of the master equation to rate equations between quantum levels for the atomic motion in the optical potential wells, as presented in Sec. V. We now compare the results of these two methods with the more exact numerical implementation of the master equation discussed in Sec. IV.

The mean kinetic energy E_K of the atomic distribution and the population π_0 of the ground state for the atomic motion obtained by the semiclassical Monte Carlo calculations and the integration of the master equation are shown in Fig. 14 for a typical experimental value of the detuning $\Delta = -5$. The agreement observed in the figure is very good, although the semiclassical calculations relied upon a drastic simplification of the momentum diffusion tensor. For the semiclassical results in Fig. 14, we used the same truncation in momentum space as in the quantum calculation. This truncation has been chosen large enough to keep the boundary effect small on π_0 as discussed in Sec. III D. Note that the corresponding boundary effect on E_K is dramatic: as shown in Sec. III C, $\langle p^2\rangle$ is indeed diverging for $u_0 < 200$ in the absence of truncation.

We know from the secular approach that for a large value of $|\Delta|$, resonances in the population π_0 as a function of u_0 appear. The observability of these resonances has been investigated by the integration of the master equation for increasing values of $|\Delta|$. These results are shown in Fig. 15 together with the prediction of the secular approach. The results for the calculations within the secular approach were obtained for the type of bound-

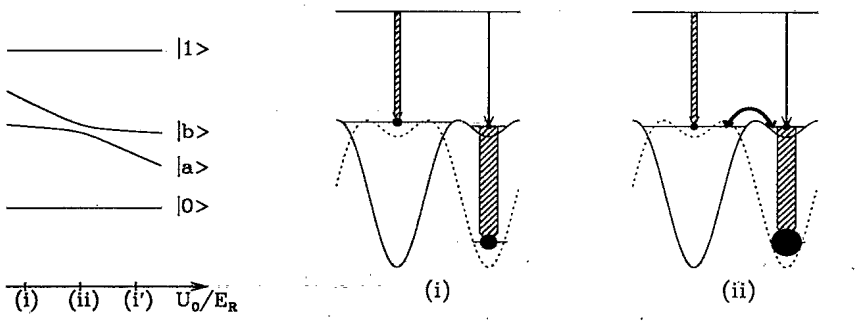

FIG. 13. Simple model to demonstrate the effect of an avoided crossing on the population of the ground state π_0. The states $|a\rangle$ and $|b\rangle$ symbolize the two spatial components of the eigenstates of U_+ participating in the avoided crossing: $|a\rangle$ is located in the small potential well of U_+ [i.e., around $(x, y) = (0, \lambda/2)$] and $|b\rangle$ is located in the large potential well of U_+ [i.e., around $(x, y) = (0, 0)$]. $|0\rangle$ is the ground state of U_- and $|1\rangle$ stands for the rest of the states in the problem, i.e., mainly excited states of U_+. In (i) and (i') the components $|a\rangle$ and $|b\rangle$ do not mix in the eigenstates and the feeding of the ground state is rather weak. On the contrary, at the center of the avoided crossing in (ii), the two components $|a\rangle$ and $|b\rangle$ mix and this mixing leads to an increased population in the ground state.

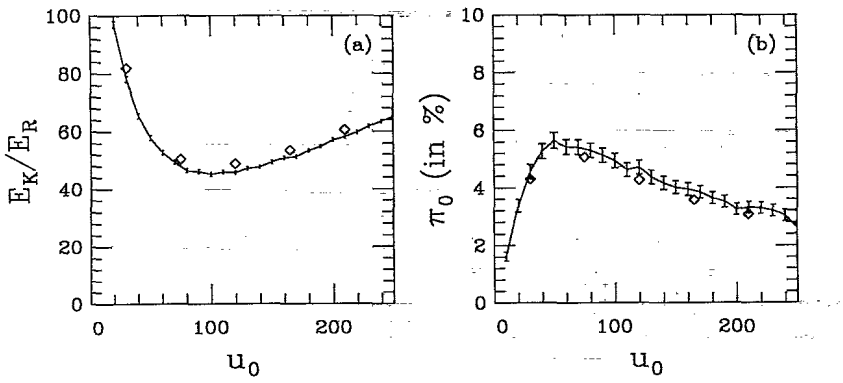

FIG. 14. Comparison of the results for the calculations within the semiclassical approach (error bars) and the more exact numerical integration of the master equation ($\diamond$). (a) The mean kinetic energy $E_K = \langle p^2 \rangle / 2M$ in units of the recoil energy E_R and (b) the population π_0 of the ground state of the atomic motion. In both calculations, we had a truncation in momentum space $n_{\max} = 15$ [as in Eq. (31)] and a detuning $\Delta = -5$.

ary conditions and the Bloch vector of Sec. IV, which are different from the ones used in Sec. V. However, the large values of $|\Delta|$ force us to use very small time steps dt in the numerical integration of the master equation. In both the secular and the master equation approaches, we therefore restrict ourselves to a smaller value of the cutoff parameter: $n_{\max}$ [as defined by Eq. (31)] is only 8, instead of 15 in the previous calculations. The important result concerns the minimum detuning for which the resonance may be observed. A detuning $|\Delta| \geq 50$ is required for having a change of π_0 at resonance of 20%. For detunings in usual experimental conditions (i.e., $|\Delta| \leq 20$) the resonances are washed out.

We have also tried a simple improvement of the secular approach. It consists in the inclusion of nondiagonal density matrix elements between eigenstates participating in the avoided crossing. Indeed we expect from the discussion of Sec. V that these density matrix elements represent the most important correction to the secular treatment. This is confirmed by the results shown in Fig. 15, where excellent agreement is found with the results obtained from the density matrix evolution.

In Sec. V, we have interpreted the resonances in π_0 as a pure quantum effect involving the tunneling through a barrier in the optical potential wells. As a consequence, we expect this resonance to be absent in the semiclassical predictions. We therefore compare the predictions of the improved secular method with a Bloch vector $\vec{q} = \vec{0}$ and a cutoff $n_{\max} = 15$ to the classical calculations for the same cut-off parameter $n_{\max} = 15$. We see in Fig. 16 that even for $\Delta = -100$, no resonance appears in the classical results. Note that the values of π_0 given by the classical Monte Carlo method in Fig. 16 are a bit larger than the ones given in Fig. 5(b); this is due to the larger values of the detuning in Fig. 16, which lead to colder atomic distributions.

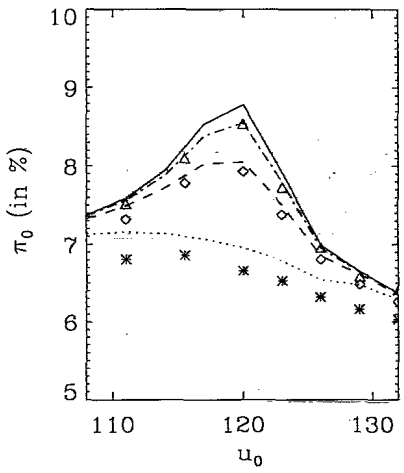

FIG. 15. The appearance of the resonance in π_0 as the value of $|\Delta|$ increases. We compare the prediction of the integration of the complete master equation with the results of the "modified" secular approach, including the nondiagonal density matrix elements between the states participating in the avoided crossing. The symbols show the results for the integration of the master equation, $\delta = -20\Gamma$ ($*$), $\delta = -50\Gamma$ ($\diamond$), and $\delta = -100\Gamma$ ($\triangle$). The lines give the corresponding curves for the "modified" secular approach as dotted, dashed, and dot-dashed lines for $\delta = -20\Gamma, -50\Gamma, -100\Gamma$. The solid line shows the result of the "pure" secular approach, corresponding to an infinite detuning. Note that the Bloch vector is $\vec{q} = \vec{0}$ (as in Sec. IV) and that the cutoff parameter in momentum space is $n_{\max} = 8$ only.

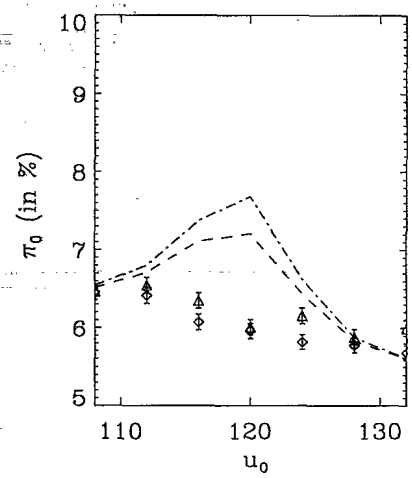

FIG. 16. Comparison between semiclassical and quantum calculations of π_0. The semiclassical results are obtained with the evolution of 64 000 atoms, with a truncation in momentum space corresponding to the cutoff parameter $n_{\max} = 15$. The detuning is $\delta = -50\Gamma$ ($\diamond$) and $\delta = -100\Gamma$ ($\triangle$). No resonance appears, even at large detuning. The quantum results are obtained from the "modified" secular approach, with a Bloch vector $\vec{q} = \vec{0}$ and the same cutoff parameter $n_{\max} = 15$. The detuning is $\delta = -50\Gamma$ for the dashed line and $\delta = -100\Gamma$ for the dot-dashed line. The resonance is clearly visible.

VII. CONCLUSION

In the preceding section, we compared the results of the three different approaches used in this paper. As a conclusion, we wish to discuss their qualitative features.

With the semiclassical approach, we are able to find a reliable value for the mean kinetic energy since we are not subject to a truncation in momentum space. This is not the case for the quantum treatments used in this paper and in [11]. Our semiclassical treatment could also easily give access to quantities such as the spatial diffusion in the optical lattices [20] and fluorescence spectra; cf. the 1D calculations in [21]. The problem with the type of semiclassical approach we have presented is that it strongly relies on the absence of coherence between the atomic ground-state sublevels due to the polarization of the laser electric field lying in the xy plane. Even so, the semiclassical limit of the master equation in Wigner form leads to momentum diffusion tensors with negative eigenvalues at some points in space. This required an additional approximation in order to construct a classical stochastic equation for the atomic motion. For a more general electric field or atomic transition, there seems to be presently no semiclassical alternative to the standard approach involving an adiabatic elimination of the internal atomic degrees of freedom and derivation of a Fokker-Planck equation [7,8,22]. This standard approach, however, cannot be used in the regime of the coldest atomic distributions [23] and one should turn to a quantum description of the atomic motion.

The secular approach constitutes an efficient way of decreasing the complexity of the master equation for the full atomic density matrix. This method can be applied when the dissipative broadening of the quantum levels is smaller than the spacing between them. In this regime, one can hope to have access to specific quantum features, including the effects of tunneling found in this paper. Other possible effects involve the band structure of the energy levels in the periodic optical potential [24]. On the other hand, the validity condition (64) for the secular approach in 2D for potential depths leading to efficient Sisyphus cooling is quite restrictive and may be even worse in 3D.

Finally, the only clearly valid quantum approach for realistic experimental conditions is the numerical integration of the master equation. However, even with the use of all the symmetries in the problem, this numerical evolution of the full atomic density matrix is a very heavy numerical task which cannot be reasonably extended to 3D. An alternative numerical method is to simulate the quantum master equation using stochastic wave functions, as an application of the general methods detailed in [25–29]. This approach has the advantage of evolving much smaller objects than the density matrix. The statistical uncertainty of the results limits the precision in the evaluation of local quantities such as the population of a single quantum state, but encouraging preliminary results for the kinetic energy [30] and the momentum distributions in 3D cooling using the Monte Carlo wave function approach of [26] have been obtained.

ACKNOWLEDGMENTS

We wish to thank C. Cohen-Tannoudji and C. Salomon for fruitful discussions and P. Zoller and R. Dum for the communication of their results on 2D laser cooling before publication. We are grateful for the allocation of time on the CRAY YMP computers of the French IDRIS, the Max-Planck Institute in Garching, and NIST in Gaithersburg, where part of the numerical calculations were performed. Finally, we acknowledge financial support from the French Collège de France, the German Alexander-von-Humboldt Foundation, the Japanese NEDO, the Danish National Research Council, and the Danish Research Academy. Laboratoire Kastler Brossel is a Unité de Recherche de l'Ecole Normale Supérieure et de l'Université Paris 6, associée au CNRS.

APPENDIX A: MASTER EQUATION IN 2D

In this appendix, we present the equation of motion for the atomic density matrix $\bar{\rho}$ describing the dynamics of the internal atomic degrees of freedom and the atomic motion in the xy plane. This density matrix $\bar{\rho}$ is deduced from the density matrix ρ for the full 3D atomic motion by taking the trace over the external atomic variables along z:

$$\bar{\rho} = \mathrm{Tr}_z[\rho] = \int dp_z \, \langle p_z|\rho|p_z\rangle \, , \tag{A1}$$

where the momentum representation along z is taken as an example.

1. The spontaneous emission kernel

In the master equation for ρ, this trace over z changes only the terms feeding the ground-state components ρ_{gg} by spontaneous emission from the excited-state components ρ_{ee}. These terms can be derived from the procedure given in [31]:

$$\left(\frac{d}{dt}\rho_{gg}\right)_{\mathrm{SE}} = \frac{3\Gamma}{8\pi}\int d^3\vec{n} \sum_{\vec{\varepsilon}\perp\vec{n}} \left(\vec{\Delta}^{(-)}\cdot\vec{\varepsilon}^{\,*}\right) e^{-ik\vec{n}\cdot\vec{r}} \times \rho_{ee} e^{ik\vec{n}\cdot\vec{r}} \left(\vec{\Delta}^{(+)}\cdot\vec{\varepsilon}\right) \delta(|\vec{n}|-1) \, . \tag{A2}$$

They involve a sum over the momentum $\hbar k\vec{n}$ and the polarization $\vec{\varepsilon}$ of the fluorescence photon. The δ function in (A2) ensures that the fluorescence photons have a wave vector of modulus k. The atomic recoil after spontaneous emission is taken into account by the translation operators $\exp(\pm ik\vec{n}\cdot\vec{r})$ in momentum space. In (A2), $\vec{\Delta}^{(\pm)}$ is the raising or lowering part of the atomic dipole operator, reduced by the atomic dipole d, with $\Gamma = d^2\omega_0^3/3\pi\varepsilon_0\hbar c^3$, such that the matrix elements of the spherical components Δ_q are Clebsch-Gordan coefficients in the standard basis: $\langle J_e m_e|\Delta_q|J_g m_g\rangle = (J_e m_e|1 J_g q m_g)$. The sum over polarizations $\vec{\varepsilon}$ is easily carried out in (A2):

$$\sum_{\vec{\varepsilon}\perp\vec{n}} \left(\vec{\Delta}^{(-)}\cdot\vec{\varepsilon}^{\,*}\right)\rho_{ee}\left(\vec{\Delta}^{(+)}\cdot\vec{\varepsilon}\right) = \sum_{i=x,y,z}\Delta_i^{(-)}\rho_{ee}\Delta_i^{(+)} - \left(\vec{\Delta}^{(-)}\cdot\vec{n}\right)\rho_{ee}\left(\vec{\Delta}^{(+)}\cdot\vec{n}\right) \, . \tag{A3}$$

When one takes the trace of (A2) over the atomic motion along z, the terms $e^{\pm ik_z z}$ appearing in (A2) disappear because of the invariance of the trace in a circular permutation. One can then, for given components $\vec{n}_\perp$ of $\vec{n}$ in the xy plane, perform the sum over the component n_z of $\vec{n}$ along z explicitly, using

$$\delta(|\vec{n}|-1)=\frac{1}{\sqrt{1-\vec{n}_\perp^2}}\sum_{\alpha=\pm}\delta(n_z-\alpha\sqrt{1-\vec{n}_\perp^2})\ . \quad \text{(A4)}$$

We get

$$\begin{aligned}\frac{d}{dt}\bar{\rho}_{gg}=\frac{3\Gamma}{4\pi}\int d^2\vec{n}_\perp\frac{1}{\sqrt{1-\vec{n}_\perp^2}}e^{-ik\vec{n}_\perp\cdot\vec{r}}\\ \times\Bigg[\sum_{i=x,y,z}\Delta_i^{(-)}\bar{\rho}_{ee}\Delta_i^{(+)}\\ -\left(\vec{\Delta}^{(-)}\cdot\vec{n}_\perp\right)\bar{\rho}_{ee}\left(\vec{\Delta}^{(+)}\cdot\vec{n}_\perp\right)\\ -(1-\vec{n}_\perp^2)\Delta_z^{(-)}\bar{\rho}_{ee}\Delta_z^{(+)}\Bigg]e^{ik\vec{n}_\perp\cdot\vec{r}}\ . \quad \text{(A5)}\end{aligned}$$

The important point is that (A5), unlike (A3), is free of crossed terms between components of the atomic dipole operator in the xy plane and along z, i.e., terms of the form $\Delta_{x,y}^{(-)}\bar{\rho}_{ee}\Delta_z^{(+)}$. Such terms are odd functions of α and cancel after the sum over α given in (A4), which corresponds to a destructive interference between the contributions of the two possible directions of spontaneous emission $\vec{n}$ for given components $\vec{n}_\perp$ in the xy plane. In 1D, this interference effect is stronger since any crossed term $\Delta_i^{(-)}\bar{\rho}_{ee}\Delta_j^{(+)}$, with $i\neq j$, is destroyed [32].

For the particular laser configuration and atomic transition $J_g=1/2\rightarrow J_e=3/2$ studied in this paper, we therefore find that density matrix coherences between the $|+\rangle_z$ and $|-\rangle_z$ ground-state sublevels cannot be coupled by spontaneous emission to the elements diagonal in the internal state ${}_z\langle+|\rho|+\rangle_z$ or ${}_z\langle-|\rho|-\rangle_z$. This plays an important role in the possibility of associating an approximate classical stochastic process with the quantum master equation in Sec. III.

The fact that the crossed terms between xy and z vanish in (A5) is a consequence of the symmetry of the 3D spontaneous-emission feeding terms (A2) by reflection in the xy plane. The unitary operator S representing this symmetry in the atomic Hilbert space is the product of the reflection in the internal atomic space $S_{\rm int}$ and the reflection acting on the atomic motion $S_{\rm ext}$. After taking the trace over the atomic motion along z, the action of $S_{\rm ext}$ becomes trivial and the reduced feeding terms (A5) are now invariant by the action of $S_{\rm int}$ alone. Since $\Delta_{x,y}$ and Δ_z have a different parity with respect to $S_{\rm int}$, the crossed terms between xy and z are odd and cannot contribute to (A5).

In the numerical calculations of the present paper, a simplified spontaneous-emission pattern is used. In this pattern, fluorescence photons are emitted only along x,y and z axes and (A2) becomes

$$\left(\frac{d}{dt}\rho_{gg}\right)_{\rm SE}$$

$$=\frac{\Gamma}{4}\sum_{\eta=\pm}\sum_{m=x,y,z}\sum_{l\neq m}\Delta_m^{(-)}e^{-ikr_l\eta}\rho_{ee}e^{ikr_l\eta}\Delta_m^{(+)}\ . \quad \text{(A6)}$$

In this equation, η is the sign of the momentum of the photon along the l axis and the normalization factor is such that (A6) has the same trace as Eq. (A2) over all atomic variables. The previous exact discussion shows, however, that the absence of crossed terms between xy and z in (A6) is not an artifact of the simplified spontaneous-emission pattern.

2. Restriction to the ground state

When the saturation parameter s_0 given in Eq. (2) is very small, the internal atomic variables of a multi-sublevel atom in the presence of laser light are relaxing with two different time scales. The first one corresponds to the rate of spontaneous emission Γ and the second one corresponds to the rate $\sim\Gamma s_0$ of optical excitation of the atom. In the quantum master equation, the components of the density matrix involving the excited state, i.e., ρ_{ee}, ρ_{eg}, and ρ_{ge}, are relaxing with the rate Γ or $\Gamma/2$ and can therefore be adiabatically eliminated and slaved to the slower variable ρ_{gg} [12,13]:

$$\frac{d}{dt}\rho_{ee}=-\Gamma\rho_{ee}+\frac{1}{i\hbar}[V_{\rm AL}^{(+)}\rho_{ge}-\rho_{eg}V_{\rm AL}^{(-)}]\simeq 0\ , \quad \text{(A7)}$$

$$\frac{d}{dt}\rho_{eg}=(i\delta-\Gamma/2)\rho_{eg}+\frac{1}{i\hbar}V_{\rm AL}^{(+)}\rho_{gg}\simeq 0\ . \quad \text{(A8)}$$

Note that we have performed two approximations in these equations. In (A8), the coupling of ρ_{eg} to ρ_{ee} by the raising part $V_{\rm AL}^{(+)}$ of the atom-laser interaction potential is neglected, as compared to the coupling to ρ_{gg}; this relies on the assumption $s_0\ll 1$, which leads to typical ρ_{ee} matrix elements smaller than ρ_{gg} by a factor s_0 (see below). The second approximation in (A7) and (A8) omits the evolution of ρ_{ee} and ρ_{eg} due to the atomic kinetic energy during the fast relaxation time Γ^{-1}; this is legitimate when the mean kinetic energy $\langle\vec{p}^2\rangle/(2M)$ is smaller than $\hbar\Gamma$. Solving Eqs. (A7) and (A8) gives ρ_{ee}, ρ_{eg}, and $\rho_{ge}=\rho_{eg}^\dagger$ as functions of the ground-state components ρ_{gg}; one has, for example,

$$\rho_{ee}=\frac{1}{2}s_0\mathcal{V}^{(-)}\rho_{gg}\mathcal{V}^{(+)} \quad \text{(A9)}$$

with $\mathcal{V}=V_{\rm AL}/(\hbar\Omega/2)$, where Ω is the Rabi frequency of each of the running laser waves. The slow variables are then inserted into the equation for ρ_{gg}, with the simplified spontaneous-emission pattern (A6), leading to the master equation

$$\frac{d}{dt}\rho_{gg} = \frac{1}{i\hbar}\left[\frac{\vec{p}^2}{2M} + \frac{1}{2}\hbar\delta s_0 \mathcal{V}^{(-)}\mathcal{V}^{(+)}, \rho_{gg}\right]$$

$$-\frac{1}{4}\Gamma s_0\{\mathcal{V}^{(-)}\mathcal{V}^{(+)}, \rho_{gg}\}$$

$$+\frac{1}{8}\Gamma s_0 \sum_{\eta=\pm}\sum_{m=x,y,z}\sum_{l\neq m} e^{-ikr_l\eta} B_m \rho_{gg} B_m^{\dagger} e^{ikr_l\eta} \tag{A10}$$

with the notation $B_m = \Delta_m^{(-)}\mathcal{V}^{(+)}$.

In the particular laser configuration studied here, the laser electric field components are all in the xy plane and consequently $\mathcal{V}$ involves only the $q = \pm$ standard components of $\vec{\Delta}$, when z is taken as quantization axis

$$\mathcal{V}^{(+)} = \mathcal{E}_+\Delta_+^{(+)} + \mathcal{E}_-\Delta_-^{(+)} . \tag{A11}$$

The reduced $\sigma_\pm$ components $\mathcal{E}_\pm$ of the laser field are written explicitly in Eq. (6). The matrix elements of $\mathcal{V}^{(-)}\mathcal{V}^{(+)}$ and of the B_m's are readily evaluated in the basis of the eigenstates $|g,m\rangle_z$ of the angular momentum along z, using the Clebsch-Gordan coefficients. The results are given in Sec. II, with a factor i omitted for convenience in B_y in Eq. (10).

APPENDIX B: CHANNELING IN MOMENTUM SPACE

We present quantitative results on the channeling of atoms discussed in Sec. III E. A jet of atoms of high velocity v_0 (i.e., $kv_0 \gg |\delta|s_0$, assuming $|\delta| > \Gamma$) along $\vec{e}_\eta = (\vec{e}_x - \vec{e}_y)/\sqrt{2}$ is considered. First, the evolution for the momentum distribution of the jet along $\vec{e}_\xi = (\vec{e}_x + \vec{e}_y)/\sqrt{2}$ due to transverse cooling is determined. The leading terms of the mean radiative force along $\vec{e}_\eta$ and of the momentum diffusion coefficient along $\vec{e}_\eta$, as functions of the velocity v_0, are then obtained. They allow a prediction of the asymptotic behavior of the momentum distribution for large velocities along $\vec{e}_\eta$.

1. Steady-state transverse momentum distribution for a jet of atoms

Under the assumption that the atomic velocity along $\vec{e}_\eta$ has a fixed value v_0, one can obtain a closed equation for the transverse atomic distribution

$$\Pi_\varepsilon^\perp(\xi, p_\xi; \eta, t) = \int dp_\eta\ \Pi_\varepsilon(\xi, p_\xi, \eta, p_\eta, t) \tag{B1}$$

by replacing the free-flight term $\vec{v}\cdot\partial_{\vec{r}}$ in (15) by $v_\xi\partial_\xi + v_0\partial_\eta$ and by integrating (15) over p_η. For the particular value $\alpha = \pi/2$ and for the ground-state sublevel $|+\rangle$, we get

$$\begin{aligned}(\partial_t + v_0\partial_\eta)\Pi_+^\perp &\equiv L(\eta)[\vec{\Pi}^\perp]_+ \\ &= (-v_\xi\partial_\xi + \partial_\xi U_+\partial_{p_\xi})\Pi_+^\perp - \gamma_{+-}\Pi_+^\perp \\ &\quad +\gamma_{-+}\Pi_-^\perp \\ &\quad +\partial_{p_\xi}^2(D_{++}^{\xi\xi}\Pi_+^\perp + D_{-+}^{\xi\xi}\Pi_-^\perp) .\end{aligned} \tag{B2}$$

One has a similar equation for $\Pi_-^\perp$. The momentum diffusion coefficients $D_{\varepsilon\varepsilon'}^{\xi\xi}$ are deduced from the 2D momentum diffusion tensors; one has, for example,

$$D_{++}^{\xi\xi} = \frac{1}{2}(D_{++}^{xx} + D_{++}^{yy} + D_{++}^{xy} + D_{++}^{yx}) . \tag{B3}$$

Equation (B2) corresponds physically to a one-dimensional transverse cooling of the atoms in the presence of optical potentials and pumping rates depending periodically on η. After a few relaxation times of L, i.e., after a few transverse cooling times, $\vec{\Pi}^\perp = (\Pi_+^\perp, \Pi_-^\perp)$ reaches a steady state which is also a periodic function of η. It is convenient to introduce the harmonics of the $L(\eta)$ operator in (B2):

$$L(\eta) = L_0 + L_+e^{i\tilde{k}\eta} + L_-e^{-i\tilde{k}\eta} . \tag{B4}$$

For our choice of the origin of the spatial coordinates, the operators L_+ and L_- coincide.

For a large velocity v_0, Eq. (B2) can be solved perturbatively by an expansion in $1/v_0$. To order 0 in $1/v_0$, only the η-independent component of $\vec{\Pi}^\perp$ is nonvanishing and it is given by

$$\begin{aligned}0 &= L_0[\vec{\Pi}_\infty^\perp]_\varepsilon \\ &= -v_\xi\partial_\xi\Pi_{\infty,\varepsilon}^\perp - \frac{2}{3}\hbar\tilde{k}\delta s_0\varepsilon\sin\tilde{k}\xi\,\partial_{p_\xi}\Pi_{\infty,\varepsilon}^\perp + \frac{2}{9}\Gamma s_0[(1+\varepsilon\cos\tilde{k}\xi)\Pi_{\infty,-\varepsilon}^\perp - (1-\varepsilon\cos\tilde{k}\xi)\Pi_{\infty,\varepsilon}^\perp] \\ &\quad +(\hbar k)^2\Gamma s_0\partial_{p_\xi}^2\left[\frac{1}{2}\Pi_{\infty,\varepsilon}^\perp + \frac{1}{9}(1+\varepsilon\cos\tilde{k}\xi)\Pi_{\infty,-\varepsilon}^\perp\right]\end{aligned} \tag{B5}$$

with $\varepsilon = \pm$. Note that the coefficients in (B5) are simply equal to the average over η of the coefficients in Eq. (B2) and that the simplified momentum diffusion tensors (23) and (24) are considered.

The coefficients of the Fourier components $e^{\pm i\tilde{k}\eta}$ of the distribution $\vec{\Pi}^\perp$ are determined from the zeroth-order approximation $\vec{\Pi}_\infty^\perp$ and we obtain the following equation for $\vec{\Pi}^\perp$, correct to first order in $1/v_0$:

$$\vec{\Pi}^\perp = \left(1 + \frac{2}{\tilde{k}v_0}\sin\tilde{k}\eta L_+\right)[\vec{\Pi}_\infty^\perp] \tag{B6}$$

with

$$L_+[\vec{\Pi}^\perp_\infty]_\epsilon = \frac{1}{9}\Gamma s_0[(\cos\tilde{k}\xi+\varepsilon)\Pi^\perp_{\infty,-\epsilon} - (\cos\tilde{k}\xi-\varepsilon)\Pi^\perp_{\infty,\epsilon}] - \frac{2}{3}\hbar\tilde{k}\delta s_0 \sin\tilde{k}\xi\,\partial_{p_\xi}\Pi^\perp_{\infty,\epsilon} + \frac{1}{18}(\hbar k)^2\Gamma s_0(\cos\tilde{k}\xi+\varepsilon)\partial^2_{p_\xi}\Pi^\perp_{\infty,-\epsilon} \,. \quad \text{(B7)}$$

2. Longitudinal mean force and momentum diffusion coefficient

Following a technique derived in detail in [33], one can obtain a mean radiative force for the jet of atoms along $\vec{e}_\eta$. Still assuming a fixed velocity along $\vec{e}_\eta$, one multiplies the equation of evolution of the two-dimensional distribution (15) by p_η and one integrates over p_η. The evolution of the mean atomic momentum along $\vec{e}_\eta$ is given by the average of the resulting equation over the external variables ξ, p_ξ and the ground-state sublevels $\varepsilon = \pm$. One is left with

$$(\partial_t + v_0\partial_\eta)\langle p_\eta\rangle(\eta,t) = \int d\xi dp_\xi\,[-(\partial_\eta U_+)\Pi^\perp_+ - (\partial_\eta U_-)\Pi^\perp_-] = \frac{4}{3}\hbar\tilde{k}\delta s_0 \sin\tilde{k}\eta\langle\cos\tilde{k}\xi(\Pi^\perp_+ + \Pi^\perp_-) + \frac{1}{2}(\Pi^\perp_+ - \Pi^\perp_-)\rangle_{\xi,p_\xi} \,. \quad \text{(B8)}$$

When the steady-state value of the transverse distribution $\Pi^\perp_\pm$ is inserted into (B8), the right-hand side of (B8) is exactly the position-dependent mean radiative force $F^\parallel(\eta,v_0)$ along η. For fast atoms along $\vec{e}_\eta$, one can spatially average this force. Using the $1/v_0$ expansion of Eq. (B6), we then find that the only nonvanishing term is the contribution of the first line of (B7) to the $\Pi^\perp_+ - \Pi^\perp_-$ term in (B8). We get for the mean force along $\vec{e}_\eta$ to first order in $1/v_0$:

$$\langle F^\parallel(\eta,v_0)\rangle_\eta = \frac{4}{27}\frac{\hbar\delta s_0}{v_0}\Gamma s_0[1-C] \,, \quad \text{(B9)}$$

where the constant C, between -1 and 1, is defined as

$$C = \langle\cos\tilde{k}\xi(\Pi^\perp_{\infty,+} - \Pi^\perp_{\infty,-})\rangle_{\xi,p_\xi} \,. \quad \text{(B10)}$$

In the absence of spatial modulation on $\Pi^\perp_{\infty,+} - \Pi^\perp_{\infty,-}$, C is equal to 0. One then recovers the simple estimate of Eq. (18), with a factor 1/2 coming from the fact that the present calculation concerns 1D cooling along the η axis while (18) describes 2D cooling. In the presence of transverse Sisyphus cooling along ξ, we expect a position dependence of $\vec{\Pi}^\perp_\infty$ leading to a positive value of C, as argued qualitatively in Sec. III E, and a subsequent reduction of the cooling efficiency.

In order to get the asymptotic behavior of the momentum distribution along $\vec{e}_\eta$, the momentum diffusion coefficient

$$D(\eta,v_0) \equiv \frac{1}{2}(\partial_t + v_0\partial_\eta)[\langle p^2_\eta\rangle(\eta,t) - \langle p_\eta\rangle(\eta,t)^2] \quad \text{(B11)}$$

is also required and can be derived from the procedure described in [33]. Among the various contributions to the momentum diffusion, the only remaining one at large velocity is the contribution of the momentum exchanged by the atoms after each fluorescence cycle. Indeed the dominant contribution at low velocity, i.e., the fluctuations of the instantaneous force $\partial_\eta U_\pm$ experienced by the atom, vanishes at high velocity [23,33]. We obtain, after average over η,

$$\langle D(\eta, v_0=\infty)\rangle_\eta = \frac{11}{18}(\hbar k)^2\Gamma s_0\left[1 - \frac{2}{11}C\right] \,. \quad \text{(B12)}$$

3. Asymptotic behavior of the momentum distribution along $\vec{e}_\eta$

We now consider p_η as a dynamical variable, which in the limit of high velocities $v_\eta = p_\eta/M$ evolves much more slowly than the transverse variables ξ, p_ξ. These transverse variables reach a steady state which does not depend on η, p_η to lowest order in $1/v_\eta$. We can therefore approximate the wings $k|v_\eta| \gg |\delta| s_0$ of the atomic distribution by the factorized form

$$\vec{\Pi}(\xi,p_\xi,\eta,p_\eta) \sim \vec{\Pi}^\perp_\infty(\xi,p_\xi)\Pi^\parallel(\eta,p_\eta) \,. \quad \text{(B13)}$$

From the average force (B9) and diffusion coefficient (B12), a standard Fokker-Planck treatment leads to the following asymptotic behavior:

$$\Pi^\parallel(p_\eta) \sim \frac{1}{|p_\eta|^{A^\parallel}} \quad \text{(B14)}$$

with

$$A^\parallel = \frac{u_0}{33}\,\frac{1-C}{1-\frac{2}{11}C} \,. \quad \text{(B15)}$$

We now calculate C as function of u_0 in a regime where the spatial modulation of the transverse distribution $\Pi^\perp_\infty = \Pi^\perp_{\infty,+} + \Pi^\perp_{\infty,-}$ is small. As in [23], we introduce as variables in (B5) $\Pi^\perp_\infty$ and $\varphi = \Pi^\perp_{\infty,+} - \Pi^\perp_{\infty,-}$. After minor approximations, neglecting the spatial variation of the momentum diffusion coefficients in (B5) and the contribution of any diffusive term $\partial^2_{p_\xi}\varphi$, one gets

$$v_\xi\partial_\xi\Pi^\perp_\infty + F_0\sin\tilde{k}\xi\,\partial_{p_\xi}\varphi = D_0\partial^2_{p_\xi}\Pi^\perp_\infty \,, \quad \text{(B16)}$$

$$v_\xi\partial_\xi\varphi + F_0\sin\tilde{k}\xi\,\partial_{p_\xi}\Pi^\perp_\infty = -\gamma_0\varphi + \gamma_0\cos\tilde{k}\xi\Pi^\perp_\infty \,, \quad \text{(B17)}$$

with the notations $F_0 = \frac{2}{3}\hbar\tilde{k}\delta s_0$, $\gamma_0 = \frac{4}{9}\Gamma s_0$, and $D_0 = \frac{11}{18}(\hbar k)^2\Gamma s_0$. Then Eq. (B17) is solved formally. One gets, for positive velocities along $\vec{e}_\xi$, the functional dependence

$$\varphi(\xi,p_\xi) = \int_{-\infty}^{\xi}\frac{d\xi'}{v_\xi}(\gamma_0\cos\tilde{k}\xi' - F_0\sin\tilde{k}\xi'\,\partial_{p_\xi}) \times\Pi^\perp_\infty(\xi',p_\xi)e^{\gamma_0(\xi'-\xi)/v_\xi} \,. \quad \text{(B18)}$$

After elimination of φ, Eq. (B16) becomes an integro-differential equation for $\Pi^\perp_\infty$, which is solved under the assumption of a negligible spatial dependence of $\Pi^\perp_\infty$,

$$\Pi_\infty^\perp(p_\xi) = \frac{\Pi_\infty^\perp(0)}{(1+p_\xi^2/\bar{p}_\xi^2)^{A^\perp/2}} \quad \text{(B19)}$$

with, for $|\delta| \gg \Gamma$,

$$A^\perp = -\frac{1}{2}\frac{M\gamma_0 F_0}{\tilde{k}D_0} = \frac{u_0}{33}\,, \quad \text{(B20)}$$

$$\bar{p}_\xi = \frac{M}{\tilde{k}}|F_0|\sqrt{\frac{\gamma_0}{2D_0}} = \hbar k\frac{u_0}{6\sqrt{11}}\,. \quad \text{(B21)}$$

When inserted into (B18), expression (B19) leads to a position-dependent φ, allowing one to estimate C. After some algebra, we get

$$C = \begin{cases} (A^\perp - 1)/2A^\perp = (u_0 - 33)/2u_0 & \text{if } u_0 > 33 \\ 0 & \text{otherwise}\,. \end{cases} \quad \text{(B22)}$$

Since we have omitted in this calculation the position dependence of the momentum diffusion terms in (B5), we should disregard also the $2C/11$ term in Eqs. (B12) and (B15) and we obtain

$$A^\parallel = \begin{cases} \frac{1}{2}(1+u_0/33) = \frac{1}{2}(1+A^\perp) & \text{for } u_0 > 33 \\ u_0/33 = A^\perp & \text{for } u_0 \le 33\,. \end{cases} \quad \text{(B23)}$$

We can now discuss the thresholds for normalizability and for the existence of a finite momentum variance. The power law distribution $\Pi(p) \sim 1/p^A$ is normalizable if $A > 1$. At the limit of normalizability of the transverse distribution, $A^\perp$ is equal to 1, leading to $A^\parallel = 1$ in (B23), for the same value of u_0, $u_0 = 33$. The two thresholds therefore coincide.

The power law distribution $\Pi(p) \sim 1/p^A$ has a finite momentum variance $\langle p^2 \rangle$ if $A > 3$ only. Thus the corresponding threshold for the transverse distribution is $u_0 > 3 \times 33 = 99$, whereas the one for the longitudinal distribution is $u_0 > 5 \times 33 = 165$.

[1] See, e.g., J. Opt. Soc. Am. B **6** (11) (1989), special issue on laser cooling and trapping, edited by S. Chu and C. Wieman.

[2] *Frontiers in Laser Spectroscopy*, Proceedings of the International School of Physics "Enrico Fermi," Course CXVIII, Varenna, 1991, edited by T. W. Hänsch and M. Inguscio (North-Holland, Amsterdam, 1991).

[3] P. Lett, R. Watts, C. Westbrook, W. Phillips, P. Gould, and H. Metcalf, Phys. Rev. Lett. **61**, 169 (1988).

[4] C. Salomon, J. Dalibard, W.D. Phillips, A. Clairon, and S. Guellati, Europhys. Lett. **12**, 683 (1990).

[5] J. Dalibard and C. Cohen-Tannoudji, J. Opt. Soc. Am. B **6**, 2023 (1989); P.J. Ungar, D.S. Weiss, E. Riis, and S. Chu, *ibid.* **6**, 2058 (1989).

[6] Y. Castin and J. Dalibard, Europhys. Lett. **14**, 761 (1991).

[7] K. Mølmer, Phys. Rev. A **44**, 5820 (1991).

[8] J. Javanainen, Phys. Rev. A **46**, 5819 (1992).

[9] A. Hemmerich and T.W. Hänsch, Phys. Rev. Lett. **68**, 1492 (1992).

[10] V. Finkelstein, J. Guo, and P. R. Berman, Phys. Rev. A **46**, 7108 (1992).

[11] K. Berg-Sørensen, Y. Castin, K. Mølmer, and J. Dalibard, Europhys. Lett. **22** 663 (1993).

[12] C. Cohen-Tannoudji, in *Fundamental Systems in Quantum Optics*, 1990 Les Houches Lectures, Session LIII, edited by J. Dalibard, J.M. Raimond, and J. Zinn-Justin (North-Holland, Amsterdam, 1990).

[13] G. Nienhuis, in *Proceedings of Light Induced Kinetic Effects on Atoms, Ions and Molecules*, edited by L. Moi, S. Gozzini, C. Gabbanini, E. Arimondo, and F. Strumia (ETS Editrice, Pisa, 1990).

[14] Y. Castin, Ph.D. thesis, Université Paris 6, 1992.

[15] See, e.g., S. Stenholm, Rev. Mod. Phys. **58**, 699 (1986).

[16] K. Berg-Sørensen, Ph.D. thesis, Aarhus University, 1994.

[17] R. Dum and P. Zoller (private communication).

[18] J.-Y. Courtois and G. Grynberg, Phys. Rev. A **46**, 7060 (1992).

[19] J.-Y. Courtois, Ph.D. thesis, Ecole Polytechnique, Paris, 1993.

[20] T.W. Hodapp, C. Gerz, C. Furtlehner, C.I. Westbrook, W.D. Phillips, and J. Dalibard (unpublished).

[21] P. Marte, R. Dum, R. Taïeb, and P. Zoller, Phys. Rev. A **47**, 1378 (1993).

[22] J. Dalibard and C. Cohen-Tannoudji, J. Phys. B **18**, 1661 (1985).

[23] Y. Castin, J. Dalibard, and C. Cohen-Tannoudji, in *Proceedings of Light Induced Kinetic Effects on Atoms, Ions and Molecules* (Ref. [13]).

[24] M. Doery, M. Widmer, J. Bellanca, G. Viedenbregt, T. Bergeman, and H. Metcalf, Phys. Rev. Lett. **72**, 2546 (1994).

[25] N. Gisin and I. Percival, Phys. Lett. A **167**, 315 (1992); J. Phys. A **25**, 5677 (1992).

[26] J. Dalibard, Y. Castin, and K. Mølmer, Phys. Rev. Lett. **68**, 580 (1992); K. Mølmer, Y. Castin, and J. Dalibard, J. Opt. Soc. Am. B **10**, 524 (1993).

[27] H.J. Carmichael, in *An Open Systems Approach to Quantum Optics*, edited by W. Beiglböck, Lecture Notes in Physics Vol. m18 (Springer, Berlin, 1993).

[28] G.C. Hegerfeldt and T.S. Wilser, in *Proceedings of the Second International Wigner Symposium, Goslar, 1991*, edited by H. D. Döbner, W. Scherer, and F. Schröck (World Scientific, Singapore, 1992).

[29] R. Dum, P. Zoller, and H. Ritsch, Phys. Rev. A **45**, 315 (1992); R. Dum, A.S. Parkins, P. Zoller, and C.W. Gardiner, *ibid.* **46**, 4382 (1992).

[30] Y. Castin, K. Berg-Sørensen, K. Mølmer, and J. Dalibard, in *Fundamentals of Quantum Optics III*, Proceedings of the Fifth Meeting on Laser Phenomena, Küthai, Austria, 1993, edited by F. Ehlothzky (Springer-Verlag, Berlin, 1993).

[31] C. Cohen-Tannoudji, in *Frontiers in Laser Spectroscopy*, 1975 Les Houches Lectures, Session XXVII, edited by R. Balian, S. Haroche, and S. Liberman (North-Holland, Amsterdam, 1975).

[32] Y. Castin, H. Wallis, and J. Dalibard, J. Opt. Soc. Am. B **6**, 2046 (1988).

[33] K. Berg-Sørensen, Y. Castin, E. Bonderup, and K. Mølmer, J. Phys. B **25**, 4195 (1992).